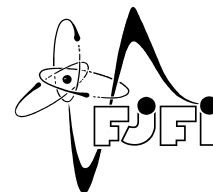




CZECH TECHNICAL UNIVERSITY IN PRAGUE
Faculty of Nuclear Sciences and Physical Engineering
Department of Physics



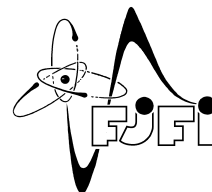
Research project

Preparation for a measurement of diffraction processes
in the ATLAS experiment

Author: **Bc. Dagmar Bendová**
Supervisor: **Mgr. Marek Taševský, PhD.**
Academic year: 2016/2017



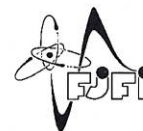
ČESKÉ VYSOKÉ UČENÍ TECHNICKÉ V PRAZE
Fakulta jaderná a fyzikálně inženýrská
Katedra fyziky



Výzkumný úkol

Příprava na měření difrakčních procesů v experimentu
ATLAS

Autor: **Bc. Dagmar Bendová**
Vedoucí práce: **Mgr. Marek Taševský, PhD.**
Akademický rok: 2016/2017



Katedra: fyziky

Akademický rok:

2016/2017

VÝZKUMNÝ ÚKOL

Student: Bc. Dagmar Bendová
Obor: Experimentální jaderná a částicová fyzika
Vedoucí úkolu: Mgr. Marek Taševský, Ph.D., FzÚ, AV ČR, v.v.i., Praha

Název úkolu (česky/anglicky):

Příprava na měření difrakčních procesů v experimentu ATLAS
Preparation for a measurement of diffraction processes in the ATLAS experiment

Pokyny pro vypracování:

1. Navázat na výsledky bakalářské práce a srovnat předpovědi generátoru PYTHIA 8.2 pro různá nastavení parametrů s publikovanými daty experimentu ATLAS pro difrakční případy se dvěma jety.
2. Seznámit se s nově instalovaným detektorem dopředných protonů AFP v experimentu ATLAS a jeho fyzikální motivací, a to pomocí jak interních dokumentů kolaborace, tak aktuálních prezentací na konferencích.
3. Seznámit se s softwarovým rámcem v kolaboraci ATLAS pro práci na datech nabraných detektorem AFP a zapojit se do aktivit české skupiny v pracovní skupině ALFA-AFP diffraction v experimentu ATLAS.
4. Seznámit se s výpočetním systémem GRID a aktivně jej používat.
5. Vytvořit rozdělení základních vlastností případů se zadetekovaným protonem v detektoru AFP, jako jsou vlastnosti tohoto protonu (čtyř-impuls, frakce tohoto čtyř-impulsu nesená Pomeronom, ...) a systému v centrálním detektoru (čtyř-impuls, hmota, multiplicita částic a čtyř-impuls jetů).

Součástí zadání výzkumného úkolu je jeho uložení na webové stránky katedry fyziky.

Literatura:

- [1] G. Aad et al. (ATLAS Collab.): Dijet production in cm energy = 7 TeV pp collisions with large rapidity gaps at the ATLAS experiment, Phys. Lett. B754, 214 (2016).
[2] C. O. Rasmussen and T. Sjöstrand: Hard Diffraction with Dynamic Gap Survival, JHEP 1602, 142 (2016).
[3] I. Helenius, J. R. Christiansen and C. O. Rasmussen: Recent PYTHIA 8 developments: Hard diffraction, Colour reconnection and $\gamma\gamma$ collisions, arXiv:1604.07996 [hep-ph].
[4] L. Adamczyk et al.: Technical design report for the ATLAS Forward proton detector, 2015, ATLAS-TDR-024-2015.
[5] Prezentace z interního AFP review (říjen 2016).
[6] Interní Twiki stránky AFP projektu v experimentu ATLAS.
[7] M. Taševský: Status of the AFP project in the ATLAS experiment (to be published in the Proceedings of the Diffraction 2016 conference).

Datum zadání: 20.10.2016

Datum odevzdání: 30.06.2017


.....

vedoucí katedry

Prohlášení:

Prohlašuji, že jsem svůj výzkumný úkol vypracovala samostatně a použila jsem pouze podklady (literaturu, projekty, software, atd.) uvedené v příloženém seznamu.

Nemám závažný důvod proti použití tohoto školního díla ve smyslu §60 Zákona č. 121/2000 Sb., o právu autorském, o právech souvisejících s právem autorským a o změně některých zákonů (autorský zákon).

V Praze dne 22.9.2017

Dagmar Bendová

Title:

Preparation for a measurement of diffraction processes in the ATLAS experiment

Author: Bc. Dagmar Bendová

Specialization: Experimental Nuclear and Particle Physics

Sort of the project: Research task

Supervisor: Mgr. Marek Taševský, PhD., Institute of Physics of the Academy of Sciences of the Czech republic

Abstract: Diffraction represents a large contribution to the total inelastic cross-section in particle collisions. It is therefore very important to understand its nature and to develop suitable instrumentation which could provide new observations of diffractive processes in the data and information on their features. The predictions of the recent Pythia 8.2 event generator, which provide a dynamical generation of gap survival probability factor in hard diffraction, are compared to the previous version 8.1 of the generator and also to the published ATLAS data in events with at least two jets with $p_T > 20$ GeV. This research task also presents detector level distributions of events with a tagged proton with the AFP detector and jets in the central detector in the final state. The ATLAS Forward Proton (AFP) detector was recently installed at the ATLAS experiment and it is designed to identify events in which one or both protons emerged intact from the collision and at very small angles.

Key words: diffraction, rapidity gaps, jets, Monte Carlo event generator Pythia 8, ATLAS Forward Proton

Název práce:

Příprava na měření difrakčních procesů v experimentu ATLAS

Autor: Bc. Dagmar Bendová

Obor: Experimentální jaderná a částicová fyzika

Druh práce: Výzkumný úkol

Vedoucí práce: Mgr. Marek Taševský, PhD., Fyzikální ústav AV ČR, v.v.i.

Abstrakt: Difrakční procesy utvářejí značný příspěvek k neelastickému účinnému průřezu částicových srážek. Je proto velmi důležité lépe porozumět jejich podstatě a vyvinout detekční nástroje schopné zaznamenat data obsahující tyto procesy a umožnit tak zkoumání jejich vlastností. Předpovědi Monte Carlo generátoru Pythia 8.2, který umožňuje dynamicky generovat pravděpodobnost, že prázdná oblast v detektoru indikující difrakční proces nebude zaplněna měkkými částicemi, jsou srovnány s předchozí verzí Pythia 8.1. Tyto předpovědi jsou také porovnány s daty z experimentu ATLAS, ve kterých byly identifikovány případy se dvěma jety s $p_T > 20$ GeV. Dále jsou v této práci prezentována rozdělení základních vlastností případů se zadetekovaným protonem v detektoru ATLAS Forward Proton (AFP) a s jety v koncovém stavu v systému v centrálním detektoru. Dopředný detektor AFP byl v nedávné době instalován v rámci experimentu ATLAS a jeho účelem je identifikovat případy, ve kterých jsou jeden či oba z interagujících protonů rozptýleny v dopředném směru pod velmi malými úhly.

Klíčová slova: difrakce, prázdné oblasti v detektoru, jety, MC generátor Pythia 8, detektor AFP

Acknowledgment:

I would like to express my gratitude to my supervisor Dr. Marek Taševský for his guidance, corrections and his patience. I would also like to thank to Dr. Rafal Staszewski for the preparation of skimmed data and together with Ivan Lopez Paz for their many useful advice and remarks on the AFP data. Finally I would like to thank to my nearest ones for their support.

Contents

Introduction	9
1 Diffraction	10
1.1 Soft Diffraction	11
1.2 Hard Diffraction	12
2 The LHC and the ATLAS detector	14
2.1 Inner Detector	16
2.1.1 Pixel Detector	17
2.1.2 Semi-Conductor tracker (SCT)	17
2.1.3 Transition Radiation Tracker (TRT)	17
2.2 Calorimeters	17
2.2.1 Electromagnetic Calorimeters	17
2.2.2 Hadronic Calorimeters	18
2.2.3 Forward Calorimeter (FCal)	19
2.3 Muon Spectrometer	19
2.4 Forward Detectors	19
3 The ATLAS Forward Proton (AFP)	20
3.1 Detector layout	20
3.2 Current status and future prospects	21
4 Monte Carlo Generators	23
5 Jets	25
6 Comparisons of Pythia 8 simulations to ATLAS data	28
6.1 Pythia 8.1	29
6.2 Pythia 8.2	31
7 Results of the AFP data analysis	35
7.1 Trigger and event selection	35
7.2 Particle and jet properties	35
7.3 AFP results	38
Conclusion	44
Bibliography	44

Introduction

Diffractive processes are responsible for the considerable contribution to the inelastic cross-section in high-energy collisions. It is therefore very important to develop and improve its theoretical description in order to better understand the experimental results and also Monte Carlo event generators which provide valuable predictions for the experiment and allow us to compare theoretical predictions with the data. Last but not least it is crucial to improve our experimental devices in order to be able to precisely measure the desired processes.

The measurements of diffractive processes at HERA and Tevatron have provided precise results which led to the crucial improvement of the understanding the nature of diffraction. With the construction of the Large Hadron Collider at CERN new and even more precise results have been expected because the diffraction in pp collisions is now an object of interest of the large part of particle physics community as it can provide further improvements in our understanding of the Standard Model and physics beyond it. Recently the ATLAS Forward Proton (AFP) detector was installed at the ATLAS experiment and its physics program promises new and even more precise results on the diffractive processes and its properties.

A brief introduction to the theoretical description and the key properties of the diffractive processes are presented to the reader in Chapter 1. An outline of the soft diffraction phenomenology and the hard diffraction description using the means of perturbative quantum chromodynamics is provided. The Large Hadron Collider and the ATLAS experiment with its main features are described in Chapter 2. The recently installed ATLAS Forward Proton detector (AFP) and its physics program is described in Chapter 3. Chapter 4 provides an introduction to Monte Carlo event generators and briefly describes Pythia 8 generator which is later used for the simulation of diffractive events. As this research task is focused on diffractive events in which hard-scale objects called jets appear, a summary on their properties and algorithms used for their reconstruction is provided in Chapter 5.

The predictions of the Pythia 8.2 event generator and its comparison with the published ATLAS data, where diffractive processes with the production of jets were examined, are provided in Chapter 6. These predictions are also compared to the previous results of Pythia 8.1 event generator and their comparison with the data presented in author's bachelor thesis [1].

Finally in Chapter 7 a short analysis of the ATLAS data with the tagged forward protons in AFP is presented. Namely the distributions of basic kinematic features of the reconstructed calorimeter clusters and jets are provided. The tracks registered in the AFP detector are examined. Finally the fractional momentum loss and rapidity gap size distributions which could provide an evidence on the presence of single diffractive processes in the data are discussed.

Chapter 1

Diffraction

Diffraction forms a significant contribution to the total cross-section of the interaction, e.g. the pp interaction cross-section. It is considered to be a quasi-elastic process in which the object with quantum numbers of vacuum is exchanged between the two interacting protons. This colorless object is called pomeron \mathbb{P} . There are two important detector features of the diffractive processes, namely the presence of the intact initial proton and large rapidity gap which accompanies it. If both initial protons stay intact, two large rapidity gaps are observed, each accompanying one forward going proton.

An essential feature of the diffractive process is the presence of so called large rapidity gap which is a region in pseudorapidity devoid of any hadronic activity.

Several types of diffractive processes can be distinguished. The most common ones can be seen in Figure 1.1. Single diffraction (SD) forms the most frequent class of diffractive processes and it is also easily detectable when compared to other types of diffraction. One of the collided protons stays intact in this process and is rescattered under the very small polar angle, thus it possess large pseudorapidity η . A large rapidity gap is formed between the rescattered proton and a final state hadronic system X which emerged from the other proton dissociated in the course of collision. Less common process is the double diffraction (DD). It is characterized by the dissociation of both interacting protons into two hadronic systems, denoted as X and Y , which are separated by a rapidity gap. A very interesting process is a central diffraction (CD) in which both of the interacting protons are rescattered and hadronic system with quantum numbers of vacuum is formed in central region, separated from the rescattered proton by the rapidity gap at each side. One can distinguish two forms of CD process, double pomeron exchange (DPE) and central exclusive production (CEP). In CEP, both pomerons go into the hard subprocess with all of their momenta and therefore only rescattered protons and the hadronic system X can be observed. On the other hand DPE is characterized by the presence of so called pomeron remnants because only a fraction of the pomerons momentum is transferred in the interaction. A multiple pomeron exchange (MPE) can also occur, yet this process is rare and very difficult to detect.

According to a momentum transfer, we can distinguish between the soft and hard diffraction. Soft diffraction occurs at small momentum transfer scales and forms a dominant fraction of diffractive processes. It is theoretically described by various phenomenological models based on Regge theory. At a hard scale, where large momenta are transferred, a perturbative QCD [2] approach can be applied. Pomeron can be then seen as an object with internal partonic structure which can be described using relevant parton distribution functions (PDF). In the means of quantum chromodynamics, parton distribution function $f_i(x, Q^2)$ determines the probability that parton i with virtuality Q^2 carries the longitudinal momentum fraction x , where x is the Björken variable.

Very important feature of this approach is that a cross-section of a certain process at the hard scale can be expressed as a convolution of PDFs of the participating partons and a corresponding sub-process cross-section. However, as will be described later in this chapter, this factorisation of the cross-section does not withstand in diffractive processes at hadron-hadron colliders, e.g. the LHC.

The diffraction provides a valuable opportunity to study low- x structure of the proton. It can also provide an environment for the creation of interesting objects such as high- p_T jets, vector bosons, heavy quarks and their resonances or even a Higgs boson.

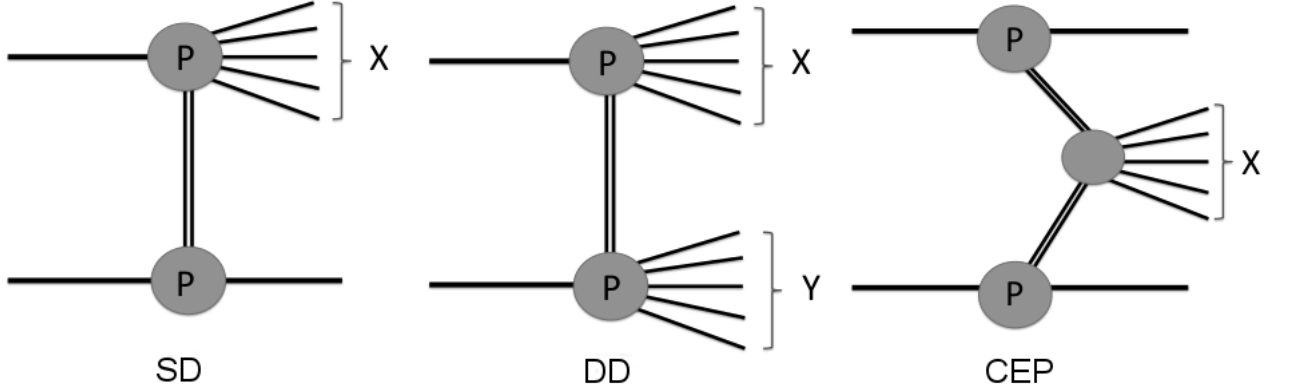


Figure 1.1: The most common types of diffractive processes. from the left to right - single diffraction, double diffraction and central diffraction. Picture taken from [3]

1.1 Soft Diffraction

As already mentioned above, a perturbative approach of the quantum chromodynamics can not be applied in soft diffractive processes due to small momentum transfer and consequent divergence of the cross-section in the perturbative series. However phenomenological models based on Regge theory [4] can be used for the successful description of the soft diffraction. Let us introduce a basic approach. Consider a single diffractive process

$$a + b \rightarrow c + X$$

in which the pomeron exchange forms the dominant mechanism. The process can be interpreted as an interaction of particle b with a pomeron radiated from particle a . Subsequently, particle b dissociates into a hadronic system X , with invariant mass M_X , and particle a is rescattered as particle c with longitudinal momentum fraction $x_L = 1 - \xi$, where ξ is the momentum fraction of particle a carried away by the pomeron. It is important to mention that ξ is very small in diffractive processes and therefore x_L is close to unity. A large rapidity gap with size $\Delta\eta$, which satisfies

$$\Delta\eta \approx -\ln \xi, \quad (1.1)$$

emerges between the particle c and the hadronic system X .

Using the process amplitude in the sense of Regge theory [4], one can calculate a factorized cross-section of the process which follows

$$\frac{d^2\sigma}{d\xi dt} = f_{\mathbb{P}/a}(\xi, t) \cdot \sigma^{\mathbb{P}b}(M_X^2, t) \quad (1.2)$$

where the first term is the pomeron flux factor which determines the probability that particle a radiates a pomeron. The second term denotes the cross-section for the pomeron scattering on particle b . Variable t is the Mandelstam variable known as squared four-momentum transfer and defined as

$$t = (p_a - p_c)^2. \quad (1.3)$$

Eq. (1.2) might suggest that pomeron can be considered as a particle. However pomeron is not a real particle. It is only considered to behave like a particle in the terms of Regge theory and subsequent phenomenological models. The detailed description of the soft diffractive phenomenology is provided in [4].

1.2 Hard Diffraction

Inner partonic structure of interacting particles can be probed at a hard scale in the processes where large momenta transfers occur. The probability that colliding proton radiates a pomeron is also based on Regge theory. However a hard diffraction pomeron has different properties than the soft one and it is considered to be a compound object like proton. Due to the hard scale its inner structure can be identified using perturbative theory and related PDFs can be determined. A diffractive parton distribution function (DPDF) $f^D(x, Q^2, \xi, t)$ can be considered as a conditional probability to find a parton i with fractional momentum $x\xi$ inside the proton which undergoes the diffractive process. The cross-section of a hard diffractive process can then be expressed as a convolution of DPDF and a cross-section $\sigma_i(x, Q^2)$ of the hard partonic sub-process

$$d\sigma = \sum_i f_i^D(x, Q^2, \xi, t) * d\sigma_i(x, Q^2). \quad (1.4)$$

The diffractive PDF can be further decomposed as

$$f_i^D(x, \xi, t, Q^2) = f_{\mathbb{P}}(\xi, t) \cdot f_i^{\mathbb{P}}(x, Q^2), \quad (1.5)$$

where first term denotes the pomeron flux $f_{\mathbb{P}}(\xi, t)$ and second one denotes the pomeron distribution function $f_i^{\mathbb{P}}(x, Q^2)$, which determines the probability to find a parton i inside the pomeron.

The deep inelastic scattering experiments performed at HERA accelerator at DESY brought important progress in understanding the hard diffraction. The NLO QCD fits ¹ [5] for gluon and quark densities were performed on diffractive DIS data.

In both of them majority of the pomeron momentum is carried by gluons at small longitudinal momentum fraction z of the proton carried by the parton interacting in certain subprocess. Quarks form a very small contribution at these momentum scales. The predictions for the behavior of diffractive processes in $p\bar{p}$ collisions at Tevatron were estimated based on the results from the HERA data. These prediction are depicted in Figure 1.2 along with the Tevatron data. The data obtained by the CDF Collaboration are clearly suppressed by a constant factor ≈ 10 when compared to the predictions based on HERA data. The suppression implies so called factorization breaking of the diffractive cross-section in hadron-hadron collision. Although it was believed that DPDFs measured at HERA are universal, it turned out to be the wrong conclusion as they can not provide proper predictions of the cross-section for diffractive hadron-hadron experiments. The observed factorization breaking was identified as the consequence of additional soft partonic interactions which spoiled the rapidity gap.

¹Denoted as "H1 2006 DPDF Fit A" and "H1 2006 DPDF Fit B".

In response to that a gap survival probability factor S^2 was introduced as a probability that the soft interactions do not spoil the gap and event survives them. The diffractive hadron-hadron cross-section was redefined as the hard diffractive scattering cross-section multiplied by the S^2 factor.

The gap survival probability was found to be $S^2 \approx 0.1$ in Tevatron single diffraction dijet events. The gap survival probability for the LHC collisions at $\sqrt{s} = 7$ TeV was predicted to be similar, according to the so called KMR model [6, 7]. Diffractive dijet measurements carried out by the CMS Collaboration [8] and compared with predictions of Monte Carlo event generators gave two compatible results

$$S^2 \approx 0.12 \pm 0.04$$

$$S^2 \approx 0.08 \pm 0.04$$

which correspond to the LO, resp. NLO, matrix elements used in those MC event generators.

The ATLAS Collaboration estimation [9] based on the comparison of the data and predictions of the MC models based on DPDFs gave result

$$S^2 = 0.16 \pm 0.04 \text{ (stat.)} \pm 0.08 \text{ (exp. syst.)}$$

which also shows a reasonable agreement with both theoretical prediction and CMS result [10].

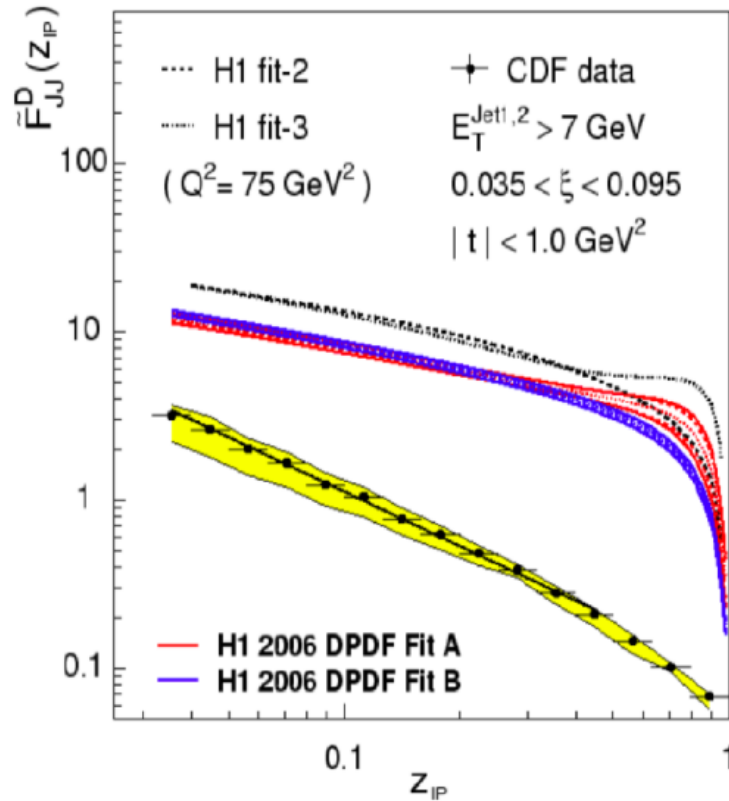


Figure 1.2: Tevatron data (yellow band) on the DPDFs as a function of the momentum fraction carried by the parton from the pomeron involved in hard sub-process compared to the predictions based on the H1 Collaboration measurements. Picture taken from [11].

Chapter 2

The LHC and the ATLAS detector

To study the predictions of the Standard Model of particle physics and explore the physics beyond, various experiments are being operated on various particle accelerators and affiliated detectors. The most powerful accelerator is the LHC which is placed in 27 km long circular tunnel near Geneva and is accompanied by a set of several smaller accelerators filling the LHC with preaccelerated protons or lead nuclei.

Inside the LHC, circulating particles collide in four interaction points where the large experiments, ATLAS, CMS, ALICE and LHCb, are placed. There are also other smaller experiments placed at the LHC which share the interaction point with one of the mentioned large detectors. The scheme of the LHC with its preaccelerators and position of the interaction points can be seen in Figure 2.1. The collider consists of two parallel beam pipes. Particles are accelerated in bunches up to the energy of 6.5 TeV per beam and after that the bunches are collided with the frequency 40 MHz. Around the beam pipes, 1232 dipole magnets are placed to bend particles along their circular trajectory. There are also 392 quadrupole magnets and several more precise magnets which focus the beam to increase a probability of the collision. The whole magnet system operates at the temperature 1.9 K which is ensured by the cooling system filled with the liquid helium.

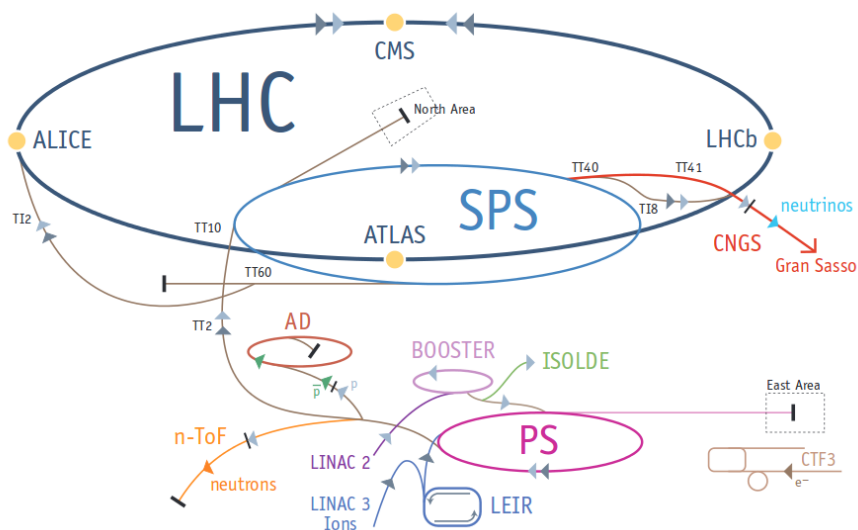


Figure 2.1: Schematic view of the CERN's accelerator system including the LHC. Taken from [12]

The ATLAS detector produces large amount of data and therefore the efficient sorting system which decides usefulness of the taken data had to be implemented. Desired events are selected using the so called Trigger System. The whole process is carried out in three steps. First of all, so called Regions-of-Interest containing possibly desired phenomena are determined using Level-1 trigger. Original calorimeters and muon spectrometer records of 40 million bunch crossings per second are reduced to approximately 100 000. After that data are transferred to the DAQ system in which a set of events is narrowed by the Level-2 trigger and then transferred to the event builder. Here, Level-3 triggers performs a detailed analysis of the event data and resulting 200 selected events which passed the event filter are transferred to the CERN computer centre for offline analysis. One copy of the data is permanently stored on tapes. All the data are also uploaded to the GRID system which provides another storage capacity and an environment for the analysis of the raw data. For the physics analysis, the ESD and subsequently xAOD data format is produced from the raw data files.

2.1 Inner Detector

Every collision produces over thousand of particles from the interaction point, creating a large track density in the detector. In order to achieve satisfactory vertex and momentum resolution for charged particles, detectors with excellent granularity have to be used to provide high-precision measurements of particle trajectories in a range matched by the precise measurements of the electromagnetic calorimeter. These features are ensured by the pixel and silicon microstrip trackers combined with the Transition Radiation Tracker. All these three detectors are independent on each other and together create the Inner Detector which extends from few centimeters to the distance of 1.2 m from the beam axis. Overall length of the ID in the z direction is 6.2 m and it covers the pseudorapidity region $|\eta| < 2.5$ and full azimuthal angle. The whole Inner Detector is immersed in a 2 T axial magnetic field produced by the Central Solenoid. The schematic view of the Inner Detector is shown in the Figure 2.3.

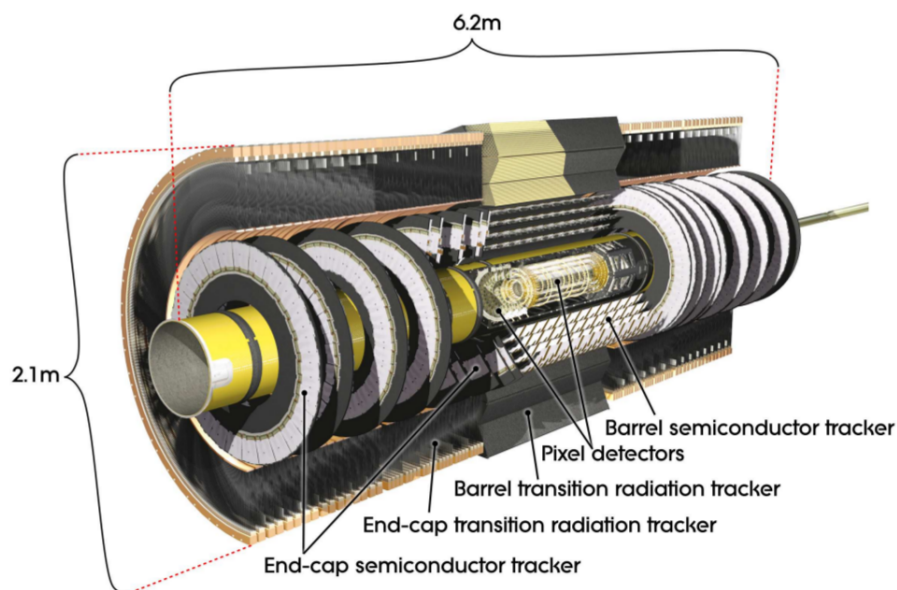


Figure 2.3: The schematic view of the ATLAS Inner Detector [13].

2.1.1 Pixel Detector

Pixel Detector creates the innermost part of the Inner Detector. It consists of four tracking layers arranged on concentric cylinders in the central region and three disks perpendicular to the beam axis in the each of end-cap regions. Due to this distribution of detection layers, Pixel Detector is capable to provide three measurement points for each particle emerging from the collision and achieves the highest granularity around the vertex region. The Pixel Detector has approximately 80 million readout channels and is composed of modules, each of them equipped by 47 232 pixels with a minimum pixel size $50 \times 400 \mu\text{m}^2$ in $(R - \phi) \times z$ dimensions. Pixel detector provides precise measurements of the primary and secondary vertex positions and also contributes to the impact parameter measurements in heavy-ion collisions.

2.1.2 Semi-Conductor tracker (SCT)

The geometrical layout of SCT, the middle component of the Inner Detector, is very similar to the Pixel Detector. It consists of four cylindrical layers and nine disks perpendicular to the beam axis in the end-cap regions. The whole SCT consists of 4088 silicon microstrip sensors. The sets of strips in the barrel layers are placed at small angles (40 mrad) to each other with one set in each layer being parallel to the beam direction (and also to the magnetic field produced by the solenoid). This provides measurements of the both $R - \phi$ coordinates. Strips in the end-cap region are running radially and there is also a set of stereo strips placed at an angle of 40 mrad. The mean pitch of the SCT strips is $80 \mu\text{m}$ and the detector is able to provide a record of four hits per track. The main purpose of the SCT is the momentum measurement.

2.1.3 Transition Radiation Tracker (TRT)

The Transition Radiation Tracker forms the outermost part of the Inner Detector enclosing the whole tracking system of the ATLAS detector. It consists of polyamide drift straw tubes, each of them is 4 mm in diameter. There are 32 000 radial straws with the length 37 cm in the end-cap region and 5000 straws with the length up to 144 cm forming the barrel TRT. The straws are filled with the mixture of xenon and carbon dioxide gas. TRT therefore combines two types of the detector. A straw tracker records tracking hits at the lower threshold and a transition radiation detector distinguishes hits which passed the higher threshold and hence enhances the electron identification capability of the ATLAS detector. Typically about 36 hits per track is recorded, allowing the TRT the precise momentum measurement for particles with pseudorapidity up to $|\eta| = 2.0$.

2.2 Calorimeters

The ATLAS calorimeter system is placed outside the central solenoidal magnet. Its purpose is to measure energy of the collision products via absorbing the incoming particle and subsequent electromagnetic or hadronic shower. Calorimeters use different techniques suited to the requirements of the studied physics processes and cover the pseudorapidity range $|\eta| < 4.9$. A cut-away view of the ATLAS calorimeters can be seen in Figure 2.4.

2.2.1 Electromagnetic Calorimeters

The electromagnetic (EM) calorimeter forms the innermost part of the whole calorimeter system and shares the vacuum vessel with the central solenoid. It is divided into a barrel part covering $|\eta| < 1.475$

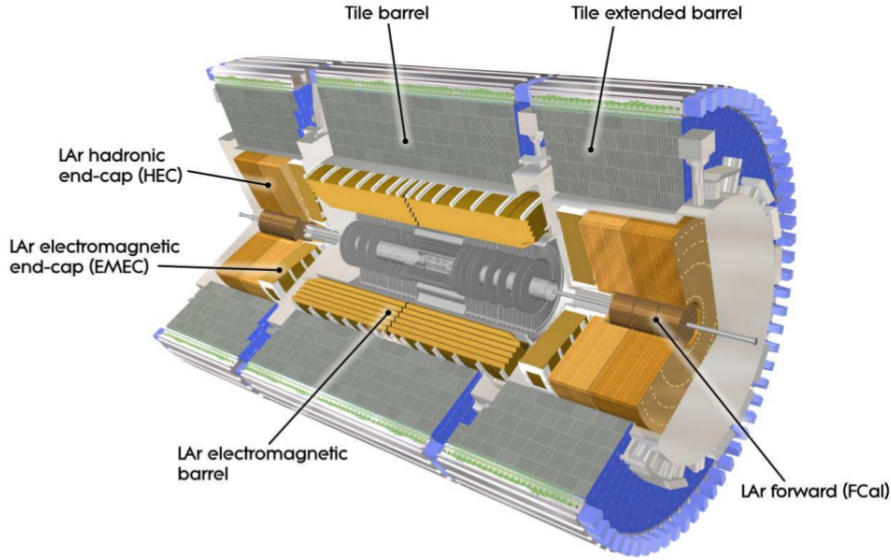


Figure 2.4: Cut-away view of the ATLAS calorimeter system [13]

and two end-cap units (EMEC) covering $1.375 < |\eta| < 3.2$, each of them immersed in their own cryostat. The barrel calorimeter further consists of two identical half-barrels, separated by a 4 mm wide gap at $z = 0$. End-cap calorimeters are formed by two coaxial wheels. The geometry of EM calorimeter provides full ϕ coverage and complete azimuthal symmetry. The EM calorimeter's purpose is to detect photons and light charged particles (especially electrons) which interact through the electromagnetic interaction. Particles entering the calorimeter deposit their whole energy into an absorber and subsequently produce an electromagnetic shower. The ATLAS EM calorimeters use lead as an absorbing material and liquid argon (LAr) as an active sampling medium filling the space between the lead plates. The total thickness of the EM calorimeter is higher than 22 radiation lengths providing a good containment for EM showers.

2.2.2 Hadronic Calorimeters

The hadronic calorimeter, as its name suggests, is supposed to detect the particles which interact via strong interaction. Hadrons deposit their energy in the calorimeter by annihilation and after that a subsequent hadronic shower is produced. The ATLAS hadronic calorimeter system consists of the tile calorimeter, extending from the inner radius of 2.28 m to the outer radius of 4.25 m, and two hadronic end-cap calorimeters (HEC) in forward directions.

The tile calorimeter is further divided into a barrel part which covers the region $|\eta| < 1.0$ and two extended barrels covering region $0.8 < |\eta| < 1.7$. It uses steel plates as an absorber and scintillating tiles as an active material.

The hadronic end-cap calorimeter is composed of two wheels at each side, located behind the EMEC. Each wheel is further segmented into two layers resulting four layers per end-cap. The HEC uses the parallel copper plates as an absorber interleaved with the liquid argon gaps as an active medium. In the pseudorapidity region, the HEC overlaps with the extended tile calorimeters and also forward calorimeter, covering the region $1.5 < |\eta| < 3.2$.

2.2.3 Forward Calorimeter (FCal)

The LAr Forward Calorimeter forms the outermost part of the end-cap calorimeter system and shares its cryostat. It covers the pseudorapidity $3.1 < |\eta| < 4.9$ and it is further divided into three modules. The module closest to the interaction point is made of copper and provides electromagnetic measurements. Other two are made of tungsten and measure the deposited energy of hadrons. The liquid argon is used as the sensitive medium in all of the modules.

2.3 Muon Spectrometer

Unlike other charged particles, muons mostly do not interact in the Inner Detector and Calorimeter system. In order to measure their trajectory and momentum, the Muon Spectrometer which forms the outermost part of the ATLAS detector is used. The measurement of the muon momentum is performed due to the deflection of its trajectory in the ATLAS outer magnet system. Muons with the pseudorapidity $|\eta| < 1.4$ are bent by the Barrel Toroid, muons with the pseudorapidity $1.6 < |\eta| < 2.7$ are bent by the two smaller end-cap magnets and in the region $1.4 < |\eta| < 1.6$, also called the transition region, both Barrel Toroids and End-cap Toroids together provide the deflection. Most of the η coverage is provided by the Monitored Drift Tubes (MDT) and at large pseudorapidities, the coverage is provided by the Cathode Strip Chambers (CSC). Apart from muon tracking, the spectrometer system also provides a trigger information. The trigger system is formed by Resistive Plate Chambers (RPC) in the barrel region and Thin Gap Chambers (TGC) in the end-cap regions. Detectors in the barrel region are installed in three cylindrical layers around the beam axis. Chambers in the end-cap regions are arranged in three layers perpendicular to the beam direction.

2.4 Forward Detectors

The ATLAS forward region is covered at both sides by four smaller detector systems.

At ± 17 m, closest to the interaction point, lies LUCID (LUminosity measurement using Cherenkov Integrating Detector). It provides online luminosity monitoring through the measurement of inelastic $p - p$ scattering.

The Zero-Degree Calorimeter (ZDC) is located at ± 140 m from the interaction point. Its main purpose is to determine the centrality of heavy-ion collisions through the detection of spectator neutrons at pseudorapidities $|\eta| > 8.3$.

The second detector used for the luminosity measurements is ALFA (Absolute Luminosity For ATLAS) which is located at ± 240 m being currently the most remote detector belonging to the ATLAS experiment. The ALFA consists of scintillating fibre trackers placed inside Roman pots. Those devices are capable to move the detection unit up to 1 mm close to the beam. It provides the information on absolute luminosity through the detection of elastic scattering products at very small angles and thus large η but currently the data with tagged protons are rather used for physics analysis of elastic and also diffractive processes.

The newest of the forward detectors is the recently installed AFP (ATLAS Forward Proton). It is located at about ± 210 m from the interaction point, however there are proposals for the second set of AFP detectors placed approximately 420 m from the IP. As the information provided by this detector plays a key role for this work, its more detailed description will be provided in the following chapter.

Chapter 3

The ATLAS Forward Proton (AFP)

The main purpose of the ATLAS Forward Proton detector is, as its name suggests, to detect very forward protons. Apart from elastic scattering, these protons originate mainly from diffractive processes. The AFP can therefore open new opportunities to identify diffractive processes by tagging very forward protons which leave the interaction region rescattered under a very small polar angle θ with respect to the beam. Rescattered protons remain inside the beam pipe but travel through it separately from the beam axis. Such protons could be detected using a very precise apparatus which enables the detection system to be brought in close proximity to the beam. Using the AFP tracking system together with the LHC optics can provide the information on momentum of the forward proton. The possibility of proton tagging would allow various measurements such as precise estimation of the rapidity gap size or double diffraction cross-section $\frac{d^2\sigma}{d\xi d|\eta|}$, measurements of the production of jets or gauge bosons in single diffractive processes, photoproduction of electroweak bosons $\gamma\gamma \rightarrow W^+W^-$ and many others physics programs [14]. It can also significantly contribute to the pile-up description and subsequent background rejection in high luminosity runs.

3.1 Detector layout

The AFP should consist of four stations placed along the beam pipe, two stations on each side of the ATLAS detector. Stations are placed between the Q5 and Q6 quadrupoles at approximately ± 206 m (Near station) and ± 214 m (Far station) from the ATLAS interaction point. Currently only stations at negative- z arm are in operation. The locations of AFP stations are shown in Figure 3.2. Each station is incorporated into the Roman pot which enables the horizontal movements of the detector and thus its insertion into the beam-pipe in close and precise proximity up to ≈ 3 mm from the beam [15]. The Roman pots can be retracted during the injection and preparation of the beam. As soon as the data taking begins, the Roman pots are moved back to its position close to the beam. The acceptance in proton relative energy loss $\xi = \frac{E-E'}{E}$, where E , E' denote the incoming and outgoing proton energy, respectively, should be around $\xi \in (0.02, 0.12)$ according to simulations [14]. Precise estimation of the AFP acceptance in ξ was not accomplished yet.

Each station is composed of four planes with radiation hard silicon 3D pixel tracking detectors. Moreover far stations are equipped with time-of-flight counters.

Each tracking plane contains 336×80 pixels compatible with the FEI4 readout system. The pixel area is $50 \times 250 \mu\text{m}$. AFP modules are based on the technology used in the ATLAS Insertable B-Layer [16] which has recently been installed into the Inner Detector system. The planes are tilted by 14° with respect to the vertical direction, i.e. they are tilted towards the x -pixel direction.

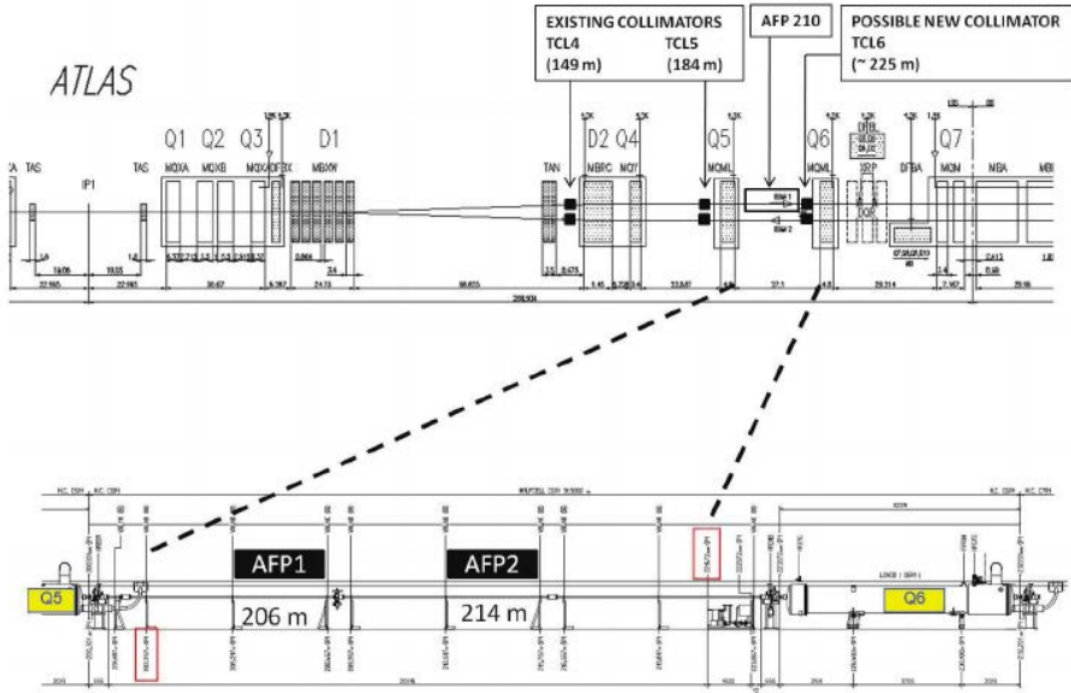


Figure 3.1: The position of the AFP stations near ATLAS. The positive- z arm is shown in the picture, the negative- z arm is nearly identical. Picture taken from [14].

This configuration allows most of the protons to pass two pixels. Therefore the hit efficiency is enhanced and a $\approx 6 \mu\text{m}$ single plane resolution along the x -axis is obtained.

The purpose of time-of-flight detectors is to identify the vertex from which the measured forward proton emerged. The ToF counters should provide a fast trigger signal which is very important in high pile-up runs. Due to its time resolution better than 10 ps and efficiency of at least 50 %, measurements in the environment with about 50 interactions per bunch crossing are possible. Time-of-flight detectors consist of L-shaped quartz bars mounted at Cherenkov angle. The scintillation light is converted into a signal using specialized Microchannel-Plate Photomultiplier tubes.

3.2 Current status and future prospects

The installation of AFP detectors is scheduled into two stages. The first stage called "AFP 0+2" took place during the winter shutdown before data taking in 2016. One arm of the AFP detector was installed at negative- z side of the ATLAS detector. The arm at positive- z side has been installed in 2017, thereby the "AFP 2+2" stage is about to be accomplished.

AFP 0+2

During the first stage of the AFP detector installation, two stations were placed in the LHC tunnel at side C ($z < 0$). The stations have been located at 206 m and 214 m from the centre of the ATLAS detector and were equipped with tracking detectors. Stations also had to pass the LHC qualification because the detector is inserted in the beam pipe and therefore has to satisfy safety requirements. Also the detector

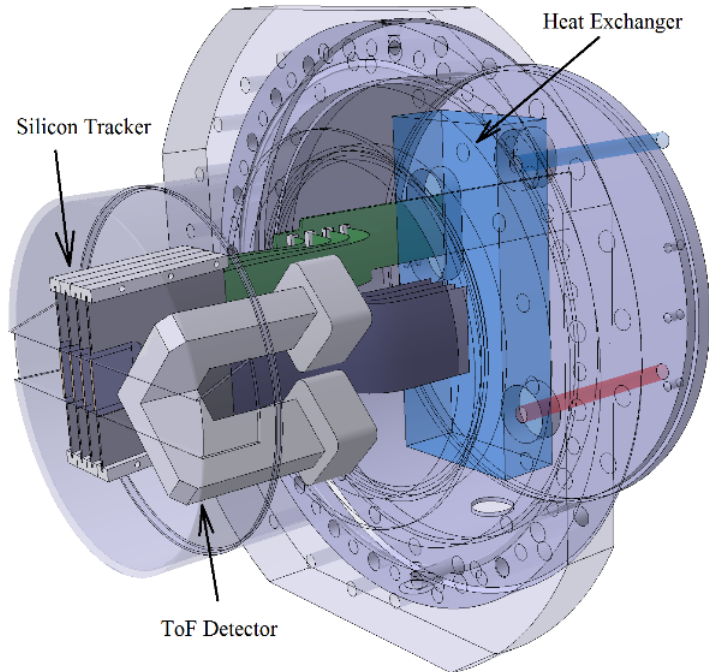


Figure 3.2: The layout of AFP tracking and ToF detectors placed in Roman pot. Picture taken from [14].

control system (DCS) and data acquisition system (DAQ) for the AFP detector had to be integrated into the ATLAS monitoring systems.

Matching physics program for this configuration is the measurement of the single diffractive dissociation using the proton tagging at $z < 0$.

During the data taking in 2016, several runs with various numbers of colliding bunches were collected. The run 310260 studied in this task belongs to runs with best efficiencies and in which all components were running more or less reliably. It comes from the so called special run with special LHC optics ensuring collection of data with low pile-up.

AFP 2+2

Other two stations have been installed at the A-side of the ATLAS detector during the winter shutdown in 2017. Replacement of the malfunctioning tracking planes was also carried out during this stage. Finally time-of-flight detectors were placed in AFP stations and integrated into the ATLAS trigger system. The final configuration of the AFP detector will allow the data taking in low and also high pile-up runs. Therefore the whole range of physics processes mentioned above (and described in detail in [14]) can be studied using the event's full kinematic provided by both ATLAS and AFP detectors.

Chapter 4

Monte Carlo Generators

Monte-Carlo generators are an important part of all experiments and also are widely used by theorists to create predictions for future experiments. They also allow us to study simulations of detector responses to the collisions at high energies. Examples of such generators are various versions of PYTHIA [17] or HERWIG [18].

In general, MC generators are based on Monte Carlo methods which obtain numerical results from repeated random sampling. MC event generators used in high-energy particle physics try to randomly generate events with the same probability as they are produced in accelerators. The typical structure of a pp collision as it is followed by the generation process is shown in Figure 4.1. The simulation of this evolution provides us the information about the whole process from the collision of beam particles to the stable final-state objects which are captured by the detectors in real collisions. As we are mostly interested in hard QCD processes, the simulation has to start in the center of collision. First of all, the probability distribution of the scatter is calculated from the perturbative QCD (pQCD). The scatter of the beam particles is followed by the parton shower which properties and evolution can still be calculated using perturbative theory. However with the time of propagation momentum scales lower down and at some point, pQCD approach is not valid anymore. During the parton shower process, the phase space is filled up with the products of the shower due to the radiation of photons by electrically charged particles through Bremsstrahlung and the radiation of gluons by particles with colour charge or by gluons themselves. As the perturbative theory can not be implemented at low momentum (or energy) scales, subsequent hadronization process has to be described using the phenomenological models such as Lund string model. During the hadronisation process, particles confine themselves into colorless hadrons which are the objects detected in real experiment. However some of the hadrons are not stable yet. The generator therefore has to contain a particle decay model which describes the behavior of the unstable hadrons and its conversion into the final-state ones. The original hard process can be also contaminated by soft particles. These are the products of multiparton interactions or rescatter of the beam remnants. These soft effects together give rise to the so called underlying event. More information on the topic can be found in [19].

Pythia 8

One of the most popular Monte Carlo high-energy collisions generators is PYTHIA. Its current versions called PYTHIA 8 are based on C++ programming language. They have been created by rewriting the previous Fortran based versions (namely PYTHIA 6) and several improvements on various physics processes and also many new aspects have been implemented in recent versions. Various models for parton shower, hadronization process, particle decay and underlying event including MPI and beam remnants behaviour are included in the program.

PYTHIA 8 therefore contains a set of physics models allowing the simulation of the above-described evolution of the collision. From our point of view, it is very important to point out that PYTHIA 8 is capable to simulate diffractive processes. Especially the newly implemented tools for the simulation of hard diffraction, which has been included in Pythia 8.2, and its impact of the PYTHIA 8 ability to describe the ATLAS data on single diffraction are one of the points of interest of this work. This new version of PYTHIA 8 should be able to provide dynamical generation of the gap survival probability factor [20]. The feature is provided by the restrictions on multiparton interactions which can otherwise fill the gap with its products and therefore the nature of the diffractive process is destroyed. More information on the properties of the PYTHIA MC generator is provided in [17].

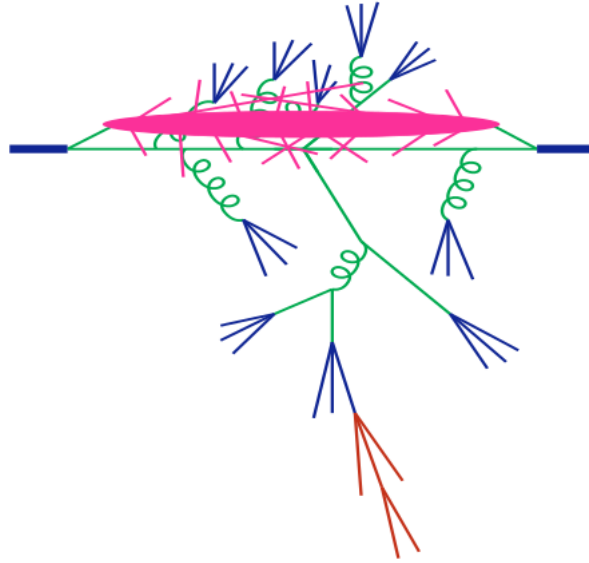


Figure 4.1: Diagram showing the evolution of a pp collision. Green colour denotes the parton shower, blue to the hadronization process, red to decay of unstable particles and pink colour corresponds to underlying event. Diagram was taken from [19]

Chapter 5

Jets

Jets represent collimated sprays of particles which are produced in hard QCD processes from initial parton, i.e. the whole jet originates in one quark or gluon. Three "levels" of jets can be distinguished based on the stage of the evolution of the collision. A parton-level jets can be identified immediately after the collision and can be linked to the partons arising directly from the collision. On this level, the perturbative QCD calculations or the parton level of MC event generators can be used to predict properties and behavior of the system. As the particles propagate themselves, they interact via strong force and create colorless hadrons. System is then described by the term particle jet or true jet. Monte Carlo generators perform their predictions of jet properties on this level. At the end of the evolution of the system, we can experimentally observe a detector level jet whose characteristics are based on detector calorimeter towers and/or on the tracks from tracking devices. They are clustered in specific regions of rapidity y and azimuthal angle ϕ , depending on the type of jet algorithm and its driving parameters.

Given jet algorithm therefore represents a link between an initial parton and detected final-state particles. Jets are completely defined by the choice of an appropriate algorithm and set of its input parameters. An ideal jet algorithm should satisfy several properties. First of all it has to fulfill all the needed theoretical requirements. The jet finding procedure has to be collinear and infrared safe. These requirements are related to the necessity of finite value of cross-section of a given process at any order of the perturbative theory. An algorithm is not infrared safe if the radiation of a soft particle changes the reconstruction result. Collinear safety ensures that jet properties remain unchanged and the jet is identified even in the situation where the original parton splits into two partons radiated parallelly to each other. An example of the effect of infrared and collinear unsafe algorithm on the result of the reconstruction can be seen in Figure 5.2. Apart from IRC safety requirements an algorithm should also be well defined, independent of the experiment and effective as we would like to obtain our results in a reasonable time.

Jet algorithms can be divided into two categories. The cone algorithms represent a "top-down" approach. They use cone of a given radius R to incorporate all the particles in surroundings of the so called seeds. Seeds represent prominent high energetic particles which are being suspected of belonging to a particular jet. The main disadvantage of cone algorithms is their possible collinear and infrared unsafety. The other type of jet algorithms are sequential clustering algorithms which represent a "bottom-up" approach. They perform the recombination of two closest objects - a jet candidate and a hadron - in momentum up to a given distance R .

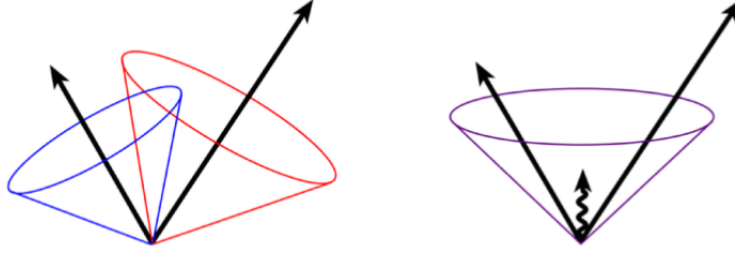


Figure 5.1: An illustration of the infrared unsafety of the jet clustering algorithm. Radiated soft particle changes number of the reconstructed jets. Picture taken from [21]

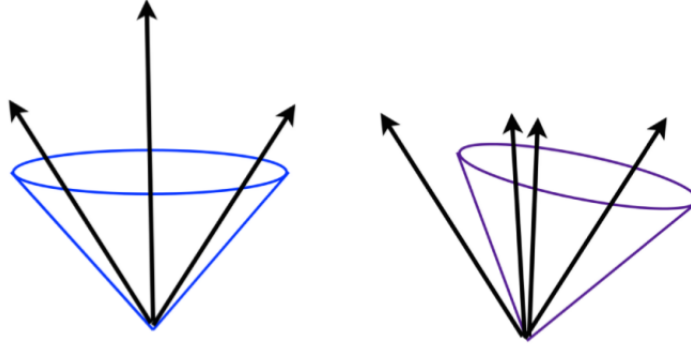


Figure 5.2: An illustration of the collinear unsafety of the jet clustering algorithm and its influence on the resultant reconstructed jet. Picture taken from [21]

The distance between the two objects i and j is defined as

$$d_{ij} = \min(k_{T,i}^{2p}, k_{T,j}^{2p}) \frac{\Delta R_{ij}^2}{R^2} \quad (5.1)$$

where $k_{T,i}$, resp. $k_{T,j}$ is the transverse momentum of particle i , resp. j , R is the jet radius and p parametrizes the type of algorithm. $p = 1$ stands for k_t , $p = 0$ for Cambridge/Aachen and $p = -1$ for anti- k_t algorithm. The quantity ΔR_{ij} is defined as

$$\Delta R_{ij} = \sqrt{(y_i - y_j)^2 - (\phi_i - \phi_j)^2} \quad (5.2)$$

with y_i , resp. y_j is the rapidity of object i , resp. j and ϕ_i , resp. ϕ_j its azimuthal angle. Also a distance between object i and the beam (B) is defined as

$$d_{iB} = k_{T,i}^{2p}. \quad (5.3)$$

The clustering algorithm evaluates which of the two distances given by Eq. (5.1) and Eq. (5.3) is smaller. If the smaller one is d_{ij} , objects i and j are recombined. If the distance d_{iB} is the smaller one, object i is labeled as a jet and it is removed from the list of candidates. Afterwards distances are recalculated for another particles i, j and process repeats until there are no objects left in the list. The advantage of

sequential clustering algorithms lies in their collinear and infrared safety, although they can be slightly slower than cone algorithms. Three introduced sequential clustering algorithms and the SISCone cone algorithm are compared in Figure 5.3. Figure shows a simulated pp event at parton-level clustered with the four above mentioned algorithms and active catchment areas of resulting hard jets. Currently the most widely used jet algorithm is the anti- k_t clustering sequential algorithm implemented in FastJet [22].

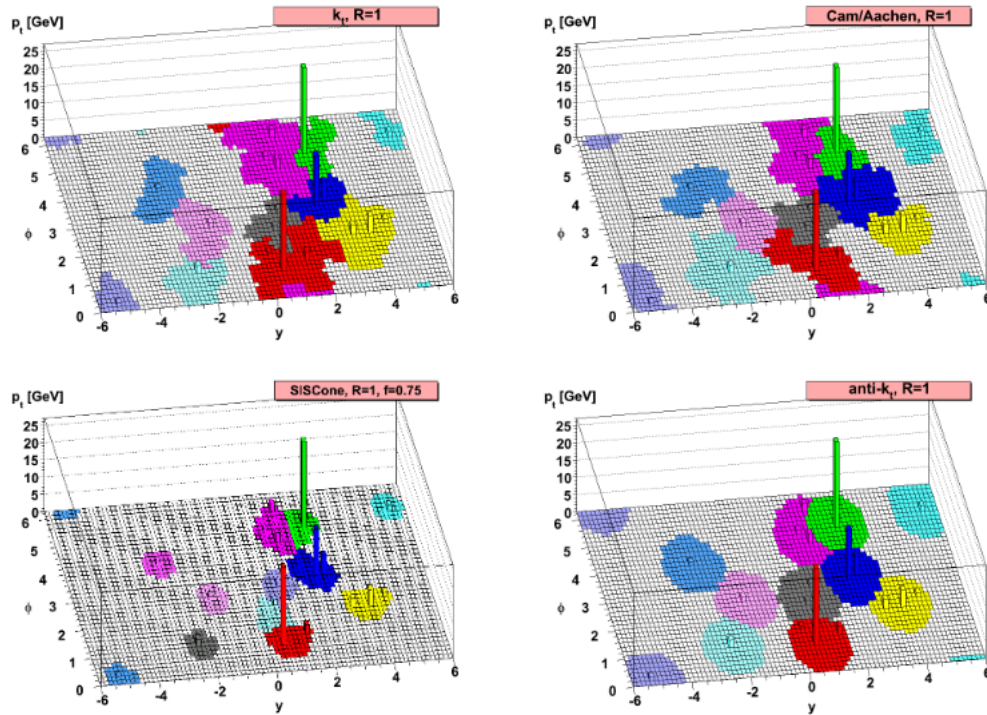


Figure 5.3: A simulated pp event at the LHC with jets reconstructed in rapidity y and azimuth ϕ phase space. Resulting hard jets clustered using k_t , Cambridge/Aachen, SISCone and anti- k_t algorithm for given radius $R = 1$ are shown. Also random soft particles called "ghosts" are depicted. Taken from [23]

Chapter 6

Comparisons of Pythia 8 simulations to ATLAS data

Large rapidity gaps (LRG) are one of the key features of diffractive processes. They emerge in the interaction due to pomeron exchange which can be interpreted as a color singlet exchange in the t -channel. The LRG is defined using the pseudorapidity η variable as the region of pseudorapidity devoid of any hadronic activity. Size of the forward rapidity gap is obtained as a distance of the first occurring particle from the edge of the detector acceptance in η . Two gaps are found using this method, one from the each side of the detector. Therefore the desired gap, which can be associated with the diffractive process, is obtained as the larger one of the two found gaps.

Fractional momentum loss ξ of the incident proton which is carried away by the pomeron is another important variable for the description of the diffractive process. It can be obtained at the detector level as

$$\xi_{cal} = \frac{1}{\sqrt{s}} \sum_i p_T^i \exp(\pm\eta^i) \quad (6.1)$$

where sum runs over all particles constituting the hadronic system X. These requirements imposed on the particles from the system X reflect the fact that ξ is obtained using the information about final state particles from calorimeter clusters at the detector level. Positive/negative sign in front of the η corresponds to the $\pm z$ direction of the intact proton. Fractional momentum loss ξ is related to the gap size through the equation 1.1.

This part of the research task results is devoted to the comparison of Pythia 8.2 predictions to published ATLAS data [9] in which dijet production in events with large rapidity gaps was studied. Obtained differential cross-sections in $\Delta\eta$ and ξ are also compared to the results of the bachelor thesis [1] where Pythia 8.1 predictions were used for the comparison with the same ATLAS data.

For this purpose, samples of pp collisions data at the center-of-mass energy $\sqrt{s} = 7$ TeV were generated using Monte Carlo generators Pythia 8.186 [17] and Pythia 8.219 [24, 25] with the pomeron flux choice of Minimum Bias Rockeffeler (MBR) flux [26, 27]. The edge of the detector in pseudorapidity is located at $|\eta| = 4.8$ in accordance with the paper [9]. Only final state particles with $p_T > 200$ MeV were accepted for the calculation of the gap size $\Delta\eta$ and the proton relative energy loss ξ . Particles with lower transverse momentum were not included with respect to the tracking acceptance of the ATLAS detector. A gap is defined as a region in pseudorapidity absent of neutral particles with $p > 200$ MeV and charged particles with $p > 500$ MeV or $p_T > 200$ MeV. The ND contribution is normalised to match the data in the first gap bin.

Samples were further processed using the data analysis framework ROOT 6.02/08 [28]. Jets were reconstructed using anti- k_t clustering algorithm [23] from the FastJet package [22] with the jet radius of $R = 0.6$. At least two jets with $p_T > 20$ GeV were required in all of the MC samples.

6.1 Pythia 8.1

The differential cross-section as a function of the gap size is depicted in Figure 6.1. The distribution was studied in detail and compared to data in [1]. The non-diffractive (ND) contribution is normalised by a factor 0.75 to match the data in the first bin. The normalisation factor is very close to the factor 0.71 applied in [9]. The main contribution to the differential inelastic cross-section is formed by the ND processes at low $\Delta\eta$. The contribution of SD and DD processes slowly balances the ND ones with the increasing gap size. The inelastic differential cross-section obtained as the sum of the contributions of ND, SD and DD processes seems to be in accordance with the exponential tendency of the data. The tendency is caused by the presence of jets which reduce the available phase space and therefore large gaps are suppressed.

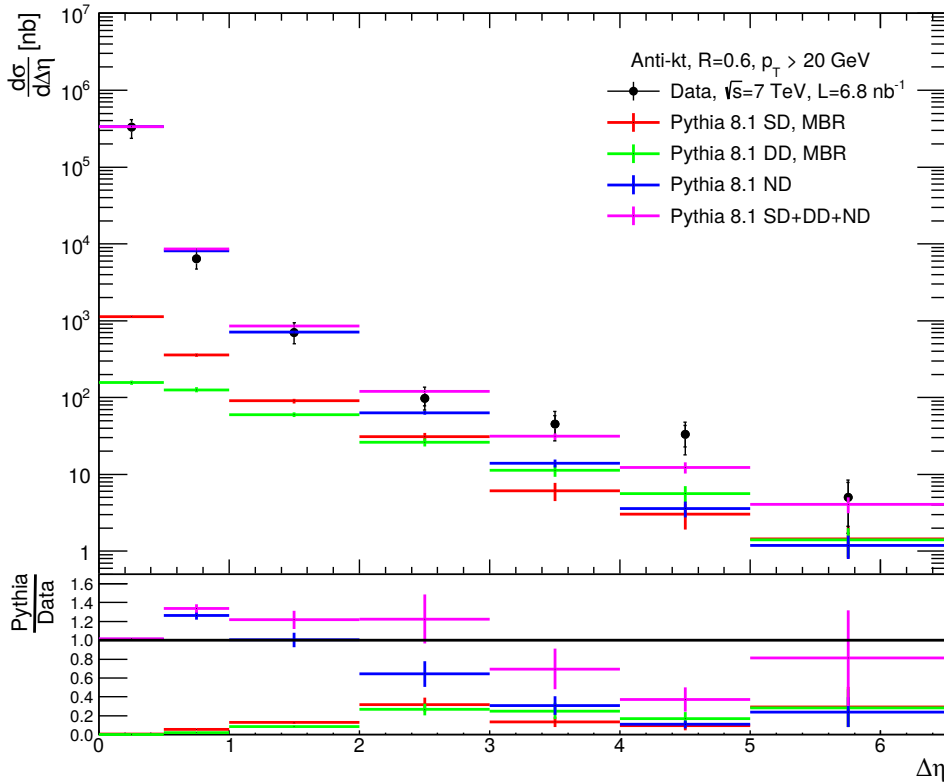


Figure 6.1: Inelastic differential cross-section in forward rapidity gap size $\Delta\eta$. At least two jets with $p_T > 20$ GeV are required and only final state particles with $p_T > 200$ MeV and $|\eta| < 4.8$ were accepted. The color lines depict predictions of Pythia 8.186 MC generator for SD, DD and ND processes and their sum. The ATLAS data [9] are represented by the black symbols.

The differential cross-section as a function of the fractional momentum loss ξ of the incident proton can be seen in Figure 6.2. The main contribution to the cross-section is formed by ND events in large values of ξ which correlates with the ND contribution to the differential cross-section in $\Delta\eta$. As ξ falls (and $\Delta\eta$ grows), the importance of diffractive components grows in such way that they are approximately equal to ND component at $\log_{10}\xi \approx -3$. Although we would expect pure domination of diffractive events in large $\Delta\eta$ and low $\log_{10}\xi$, the ND component is non-negligible even at those values.

As can be seen, all Pythia 8.1 predictions match the data and there is no need for the gap survival probability factor S^2 to be applied. It is important to note for the further analysis that all of the components were produced with multiparton interaction switch set to the default "on" option. Pythia 8.1 does not provide the possibility to exclusively generate hard diffractive processes; they need to be generated inclusively together with soft processes.

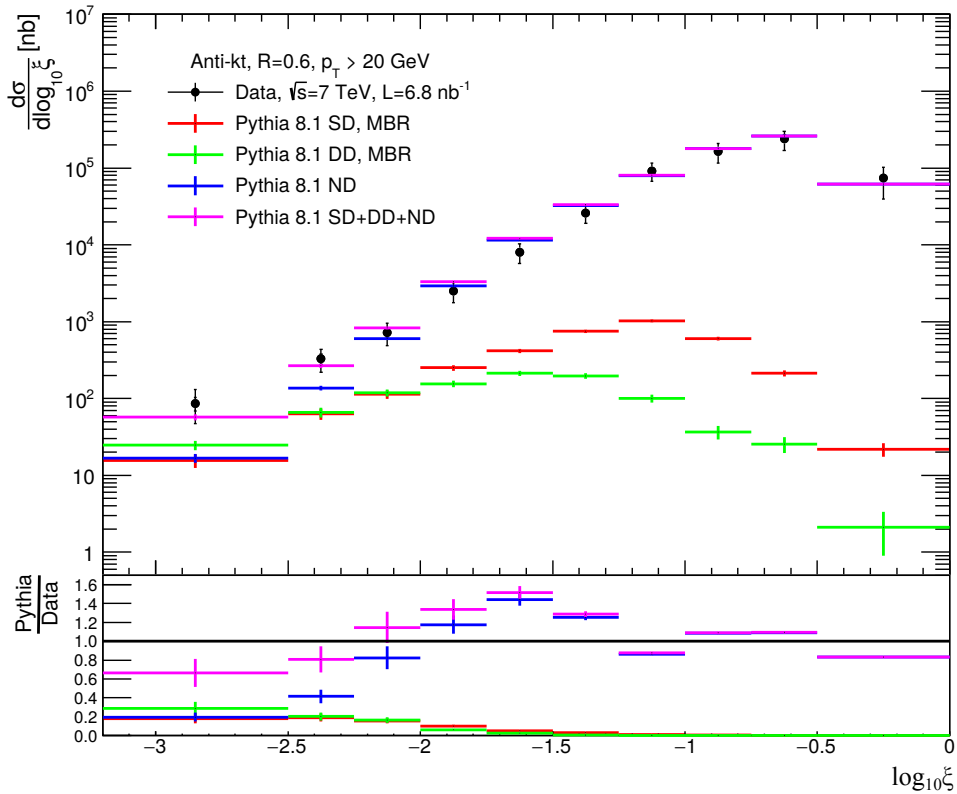


Figure 6.2: Inelastic differential cross-section in fractional momentum loss ξ of the incident proton. At least two jets with $p_T > 20$ GeV are required and only final state particles with $p_T > 200$ MeV and $|\eta| < 4.8$ were accepted. The color lines depict predictions of Pythia 8.186 MC generator for SD, DD and ND processes and their sum. The ATLAS data [9] are represented by the black symbols.

6.2 Pythia 8.2

Distributions described in previous section were resimulated using a recent Pythia 8.2 version which introduces dynamical gap survival probability factor generation in hard diffraction processes [20, 25]. The perturbative approach of the hard diffraction is available only for SD processes therefore the DD contribution presented in this section was obtained using the same soft process approach as in samples generated using Pythia 8.1. The option to include diffractive events in the hard process is available in four modes. Two of them, denoted as sample types 1 & 2 allow to generate inclusive samples of ND+SD processes with multiparton interactions switched on or switched off. Later two, denoted as sample types 3 & 4, provide the possibility to generate exclusive SD events where MPI can also be switched on or off. In the MPI-unchecked scenario the classification of hard diffraction is based solely on PDFs and the pomeron flux. For the case of MPI-off events, additional requirement on diffractive process is imposed - no extra multiparton interactions are allowed as they would destroy the rapidity gap. We will focus on the sample type 4 which provides the SD samples with the MPI parameter switched off. Also a dependence of ND contribution on the presence of multiparton interactions will be studied.

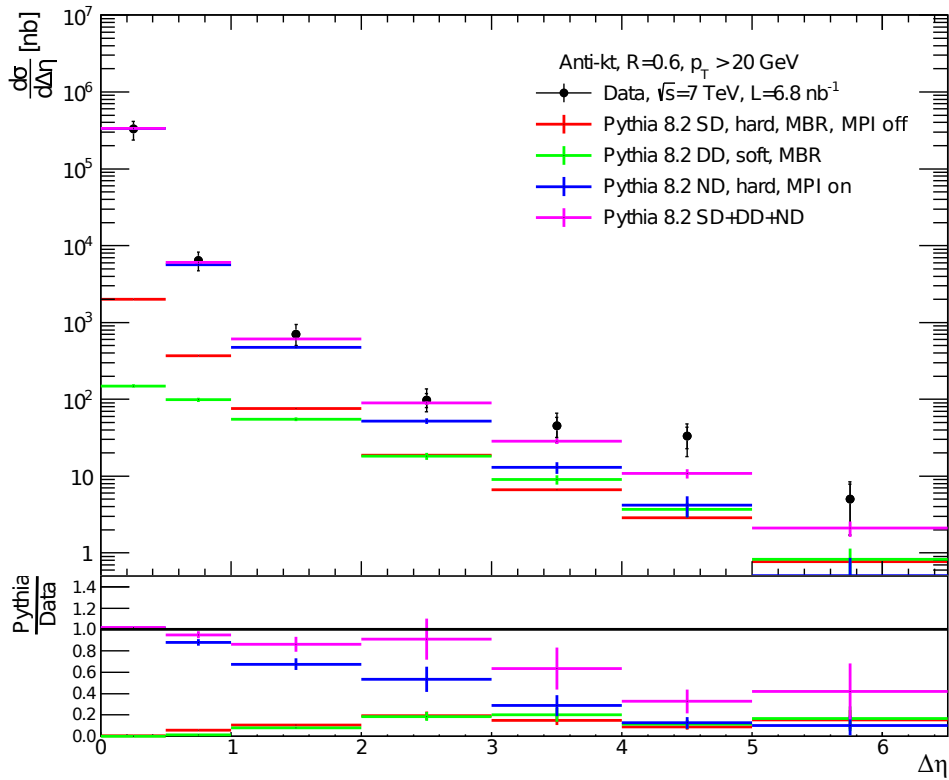


Figure 6.3: Inelastic differential cross-section in forward rapidity gap size $\Delta\eta$. At least two jets with $p_T > 20$ GeV are required and only final state particles with $p_T > 200$ MeV and $|\eta| < 4.8$ were accepted. The color lines depict predictions of Pythia 8.219 MC generator for SD, DD and ND processes and their sum. The ATLAS data [9] are represented by the black symbols. MPI was switched on in ND process and switched off in SD process.

As can be seen in Figure 6.3, the differential cross-section in $\Delta\eta$ obtained from Pythia 8.2 shows similar tendency as the differential cross-section in Figure 6.1. The hard SD process with disabled multiparton interactions does not vary significantly from the SD contribution obtained from Pythia 8.1. The ND component with enabled multiparton interactions also shows similar exponential tendency as the ND component generated in Pythia 8.1. However the MPI-on ND component obtained from Pythia 8.2 had to be normalised in the first bin by a factor of 0.87 which is different from the 0.75 factor used in previous case. The discrepancy could be explained by the fact that the relevant cross-sections slightly differ between the two version. The cross-section of non-diffractive hard process was $\sigma_{P8.1}^{ND} = (1.3260 \pm 0.0003)$ mb in Pythia 8.1 and $\sigma_{P8.2}^{ND} = (1.0950 \pm 0.0004)$ mb in Pythia 8.2. Similar agreement between the two versions of Pythia 8 can be observed in differential cross-section in ξ depicted in Figure 6.4. Despite the slight overestimation of the Pythia 8.2 SD component over the Pythia 8.1 result in large ξ values, there are no considerable discrepancies between the two versions. Therefore both versions of Pythia 8 with given set of parameters satisfactorily describe the ATLAS data [9].

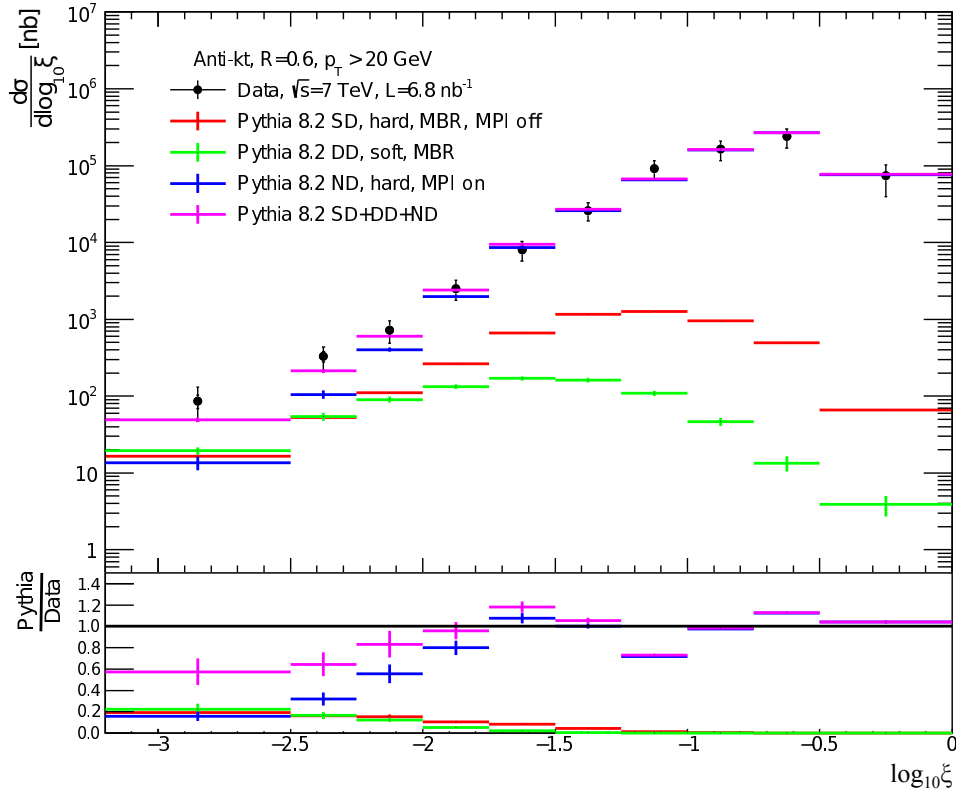


Figure 6.4: Inelastic differential cross-section in fractional momentum loss ξ of the incident proton. At least two jets with $p_T > 20$ GeV are required and only final state particles with $p_T > 200$ MeV and $|\eta| < 4.8$ were accepted. The color lines depict predictions of Pythia 8.219 MC generator for SD, DD and ND processes and their sum. The ATLAS data [9] are represented by the black symbols. MPI were switched on in ND process and switched off in SD process.

In Figures 6.5 and 6.6 the samples were obtained using MPI-off option in both SD and ND hard processes. There is clearly a huge discrepancy between the behavior of ND component in Figures 6.5 and 6.6 when compared to Figures 6.3 and 6.4 where multiparton interactions in non-diffractive hard process were enabled. Although there can be observed a possible agreement with the data in $\Delta\eta > 4$ values in Figure 6.5, most of the ND differential cross-section $\Delta\eta$ and therefore also the sum of ND, SD and DD contribution is strongly overestimated when compared to the data. In order to demonstrate the real extent of the disagreement, the ND was not normalised to the data in the first $\Delta\eta$ bin as in previous cases. The disabled MPI machinery should cause higher occurrence of the events with large rapidity gaps as there are no soft interactions which can destroy the gap. There is indeed the visible influence of this phenomenon. However the comparison with the data suggests that this approach does not give reasonable results.

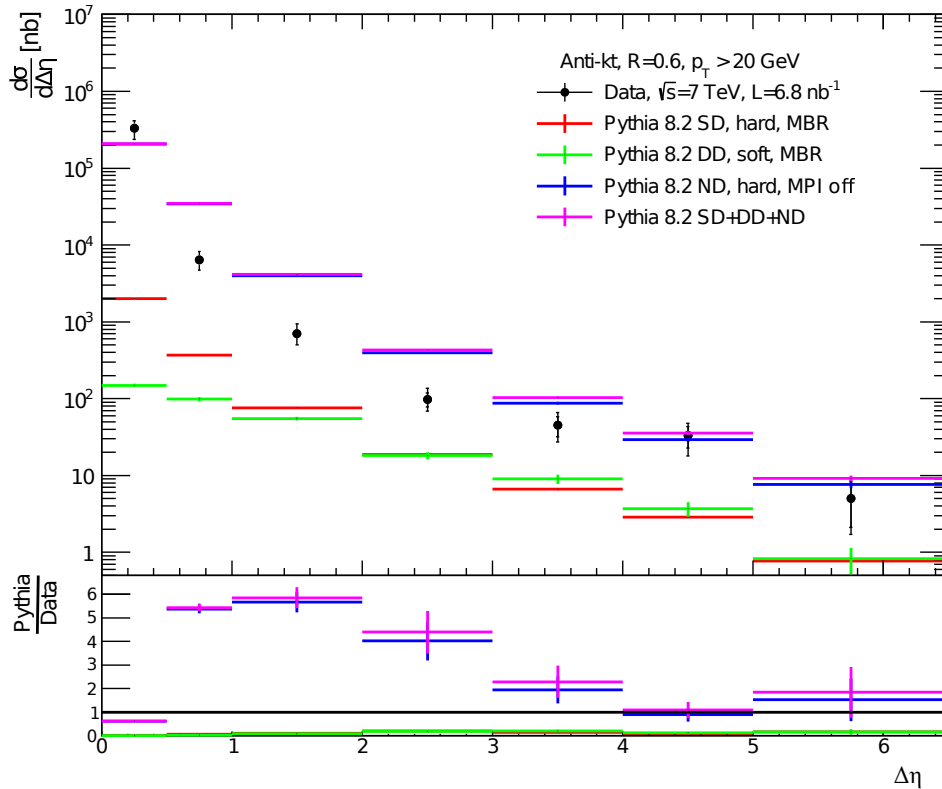


Figure 6.5: Inelastic differential cross-section in forward rapidity gap size $\Delta\eta$. At least two jets with $p_T > 20$ GeV are required and only final state particles with $p_T > 200$ MeV and $|\eta| < 4.8$ were accepted. The color lines depict predictions of Pythia 8.219 MC generator for SD, DD and ND processes and their sum. The ATLAS data [9] are represented by the black symbols. MPI was switched off in both SD and ND processes.

The behavior of the differential cross-section in the ξ depicted in Figure 6.6 also supports the observation made from the differential cross-section in $\Delta\eta$. As can be clearly seen, the ND component, which forms the main contribution to the sum of all processes in large ξ values, does not match the data at all. The maximum of the ND distribution is strongly shifted into the lower values of ξ which is caused by the increased presence of larger gaps which do not correspond to the data. Therefore it is obvious that multiparton interactions are necessary in Pythia 8 samples to provide satisfactory description of the data.

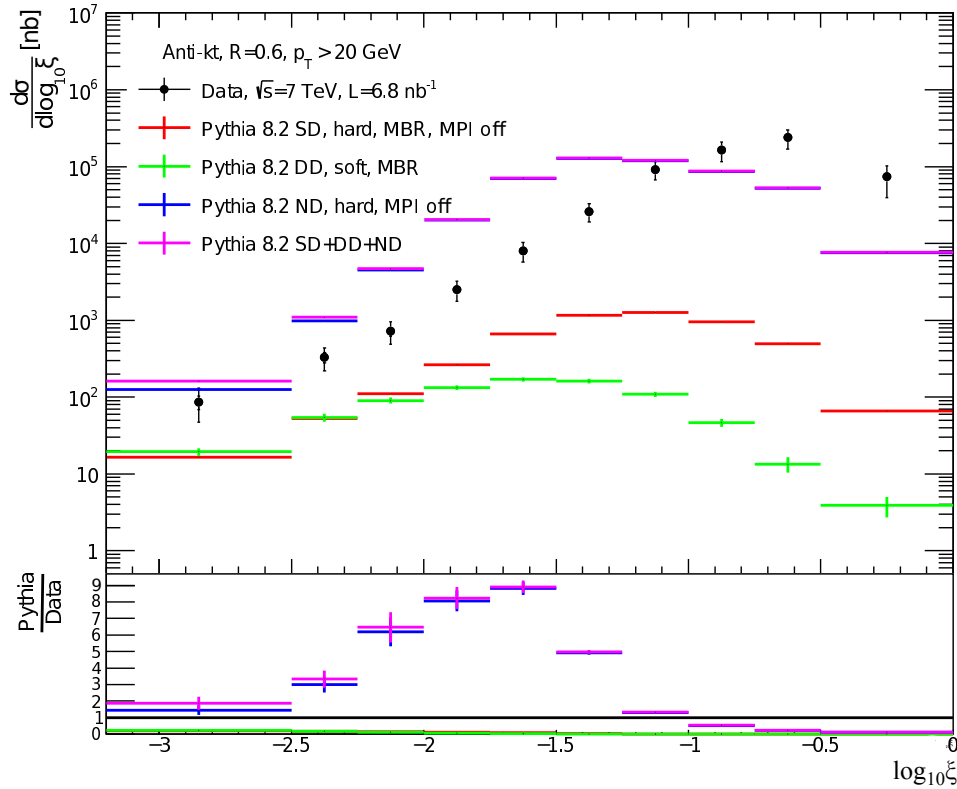


Figure 6.6: Inelastic differential cross-section in fractional momentum loss ξ of the incident proton. At least two jets with $p_T > 20$ GeV are required and only final state particles with $p_T > 200$ MeV and $|\eta| < 4.8$ were accepted. The color lines depict predictions of Pythia 8.219 MC generator for SD, DD and ND processes and their sum. The ATLAS data [9] are represented by the black symbols. MPI was switched off in both SD and ND processes.

Chapter 7

Results of the AFP data analysis

In this chapter the detector-level uncorrected distributions with jets identified in the final state are presented. The ATLAS Forward Proton detector is used as a proton tagger in the analysis. The data sample used in the analysis was collected in October 2016 during a dedicated run (310216) at centre-of-mass energy $\sqrt{s} = 13$ TeV and with low pile-up, where average number of interactions per beam crossing was $\langle \mu \rangle \approx 0.3$.

7.1 Trigger and event selection

The skimmed data used in this analysis were obtained using the HLT_noalg_L1AFP_C_J12 trigger. At least four hits (at least two per station) and a jet cluster with $p_T > 12$ GeV were required at L1 trigger level decision. More information on triggers and data quality can be found on the dedicated Twiki page [29]. Several cuts were applied to select suitable events for the analysis. To suppress the ND background, at least two hits per AFP station (at least five hits per arm) are required. Also a single reconstructed primary vertex with two associated tracks of $p_T > 100$ MeV is required to suppress the pile-up background. Events which contain more reconstructed primary vertices are rejected. Finally events are required to contain at least one jet with $p_T > 20$ GeV and $|\eta| < 3.0$ identified in the calorimeter. Jets are reconstructed from energy deposits in the ATLAS calorimeters using the anti- k_r jet clustering algorithm with the jet radius of $R = 0.4$. A requirement of $p_T > 200$ MeV was imposed on the particles reconstructed in calorimeter. The final sample consists of 328 832 events.

7.2 Particle and jet properties

First of all the basic properties of objects reconstructed in calorimeter are presented. In Figure 7.1 the distribution of the pseudorapidity of particles with $p_T > 200$ MeV reconstructed in ATLAS calorimeters are displayed. The final distribution is nearly symmetric, while the signal (SD) events are expected to be asymmetric, with a clear dominance in the region $\eta > 0$, balancing the detected proton in the AFP station which is placed at $z < 0$. The p_T distribution of the particles is depicted in Figure 7.2. We can observe a power-law character of the p_T -spectrum which is in agreement with our expectations.

The distribution of the pseudorapidity η of reconstructed jets can be seen in Figure 7.3. We can observe an evidence of small asymmetry in the η distribution. However the asymmetry is much smaller than expected and therefore we conclude that there is still considerable amount of ND background which was not successfully removed. The p_T spectrum of reconstructed jets depicted in Figure 7.4 again shows expected power-law tendency towards large values of the jet transverse momenta.

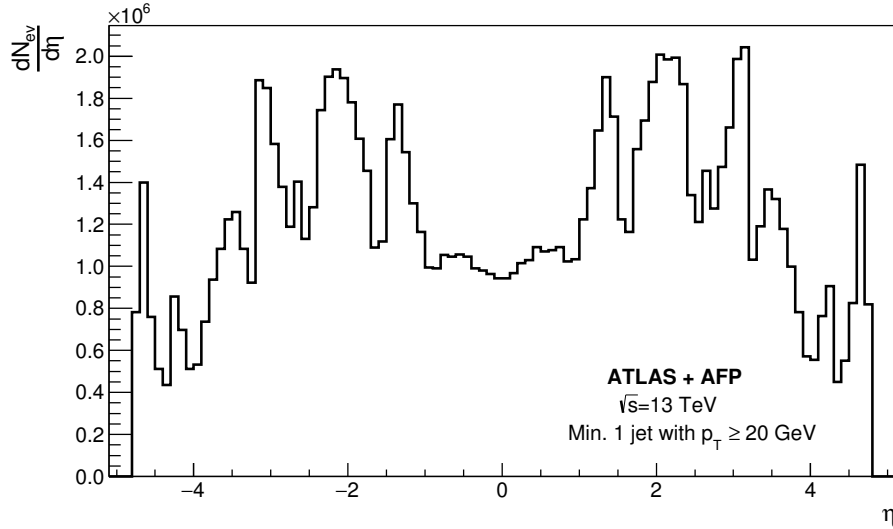


Figure 7.1: The distribution of the pseudorapidity η of particles identified in the calorimeter for events with at least one reconstructed jet with $p_T > 20$ GeV and $|\eta| < 3.0$ and particle with $p_T > 200$ MeV.

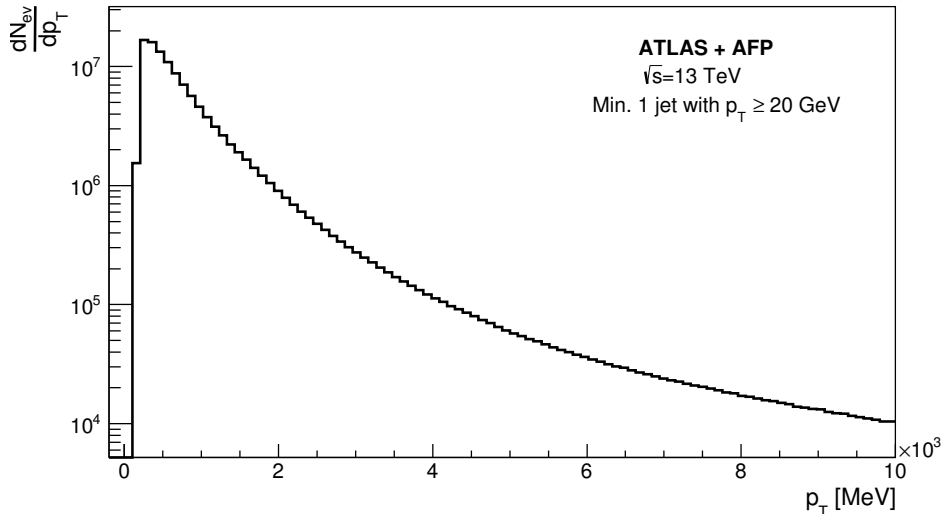


Figure 7.2: The distribution of the transverse momentum p_T of particles identified in the calorimeter for events with at least one reconstructed jet with $p_T > 20$ GeV and $|\eta| < 3.0$ and particle with $p_T > 200$ MeV.

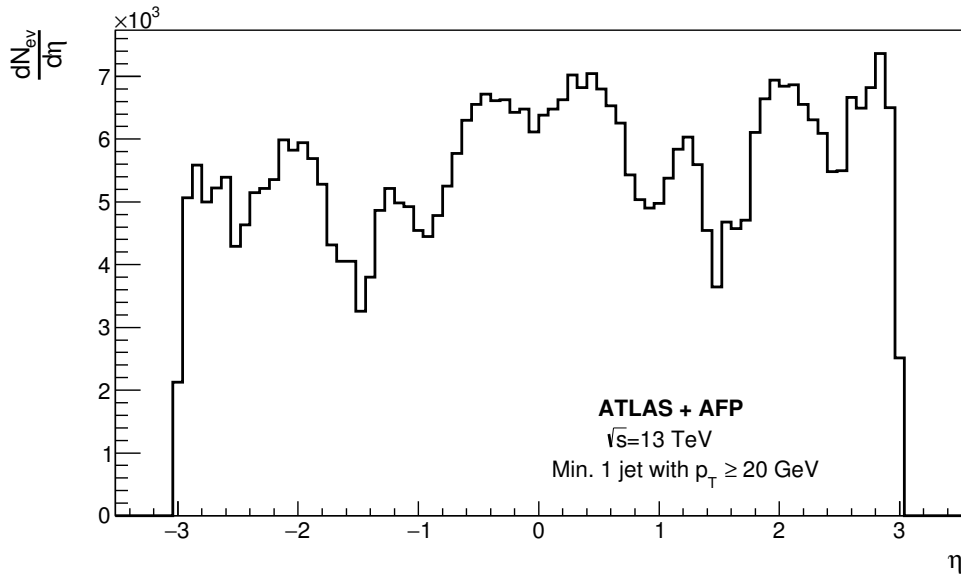


Figure 7.3: The distribution of the pseudorapidity η of jets reconstructed in the calorimeter for events with at least one jet with $p_T > 20$ GeV and $|\eta| < 3.0$ and jet constituent particles with $p_T > 200$ MeV.

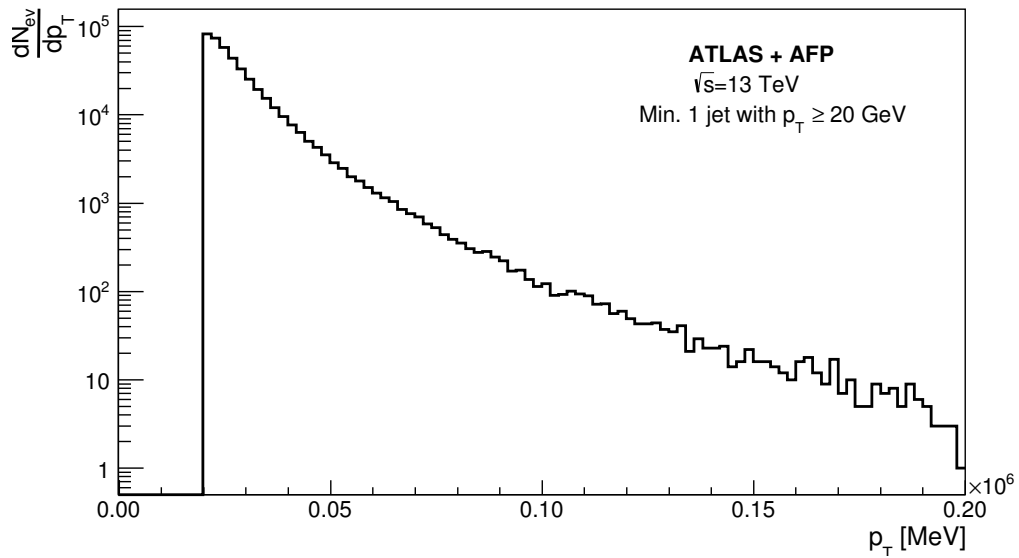


Figure 7.4: The distribution of the transverse momentum p_T of jets reconstructed in the calorimeter for events with at least one jet with $p_T > 20$ GeV and $|\eta| < 3.0$ and jet constituent particles with $p_T > 200$ MeV.

7.3 AFP results

The (x,y) distribution of the tracks registered in the Near station ($z = -206$ m) of the AFP detector is depicted in Figure 7.5. The visible structure with higher multiplicity is a consequence of the LHC beam optics which apart from beam direction and shape influences also the rescattered proton. Most of the hits caused by the forward proton is therefore expected in this region. However it is evident that large part of the distribution is still occupied by the background signal.

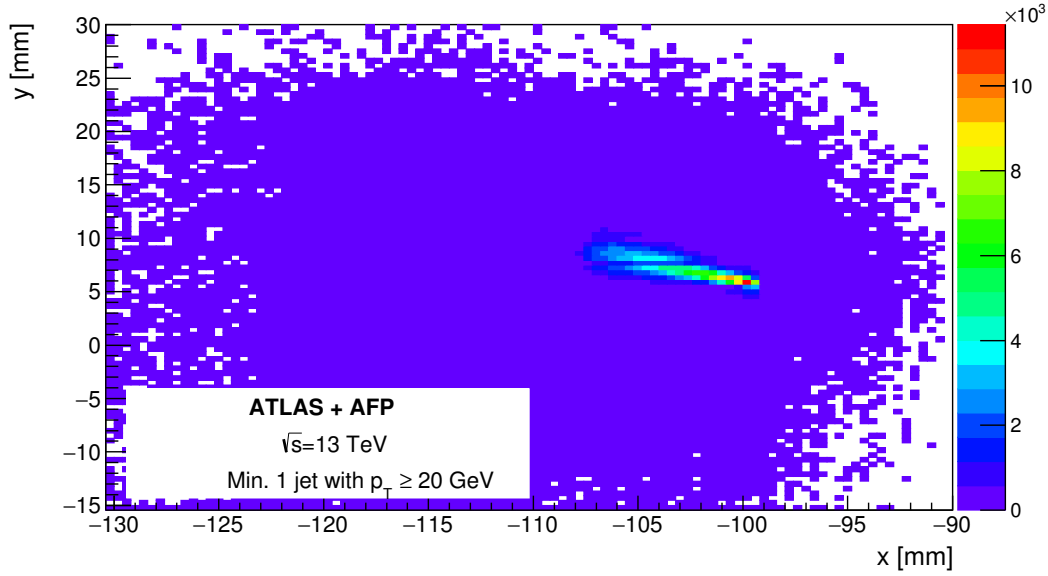


Figure 7.5: The (x,y) distribution of AFP tracks registered in the Near station ($z = -205$ m) for events containing at least one jet with $p_T > 20$ GeV and $|\eta| < 3.0$. The x -distance is measured in millimeters from the centre between the two beam pipes.

The uncorrected distribution of the detector level ξ_{cal} is shown in Figure 7.6. The fractional momentum loss of the incident proton is determined using the properties of particles reconstructed in the ATLAS calorimeter as in previous measurements [9]. The sum in expression

$$\xi_{cal} = \frac{1}{\sqrt{s}} \sum_i p_T^i \exp(-\eta^i) \quad (7.1)$$

runs over all the calorimeter clusters with $p_T > 200$ MeV. The minus sign in front of the η comes from the position of the AFP detector at $z < 0$, where the tagged protons are registered.

A clearly visible peak can be identified at $\log_{10} \xi_{cal} \approx -0.5$. From the comparison with previous results [15] shown at Figure 7.7 we can assume that this peak comes from non-diffractive processes. At larger negative values of $\log_{10} \xi_{cal}$ we can observe an evidence of possible diffractive peak analogous to the diffractive peak in Figure 7.7 located at $\log_{10} \xi_{cal} \approx -1.5$. The peak is more visible at a logarithmic scale in Figure 7.6. The confirmed presence of the diffractive peak would suggest that we are able to identify single diffractive events with the rescattered proton at $z < 0$ side of the central ATLAS detector using AFP detector to tag those forward protons. Unfortunately the dominant ND peak prevents us from such conclusions. The ND peak could possibly be reduced by further background and pile-up rejection.

The correlation between the measured ξ_{cal} of the given event and x -position of the tracks in the AFP Near station is presented in Figure 7.8. There is a visible structure with higher multiplicity at high ξ_{cal}

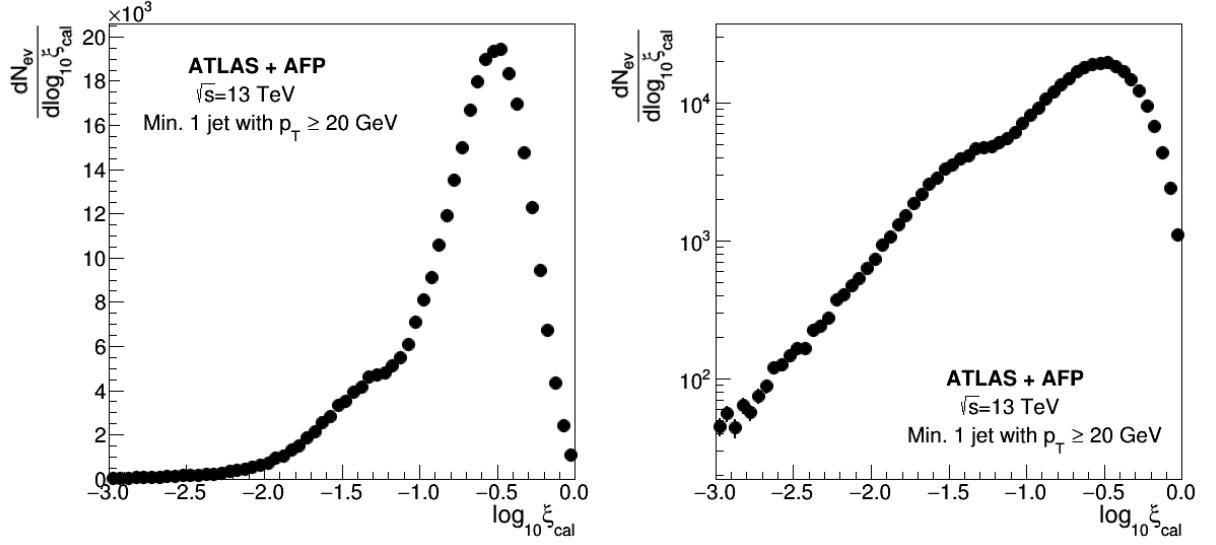


Figure 7.6: The ξ_{cal} distribution in AFP data samples on linear (left) and (logarithmic) scale. Events are required to contain at least one jet with $p_T > 20$ GeV and $|\eta| < 3.0$.

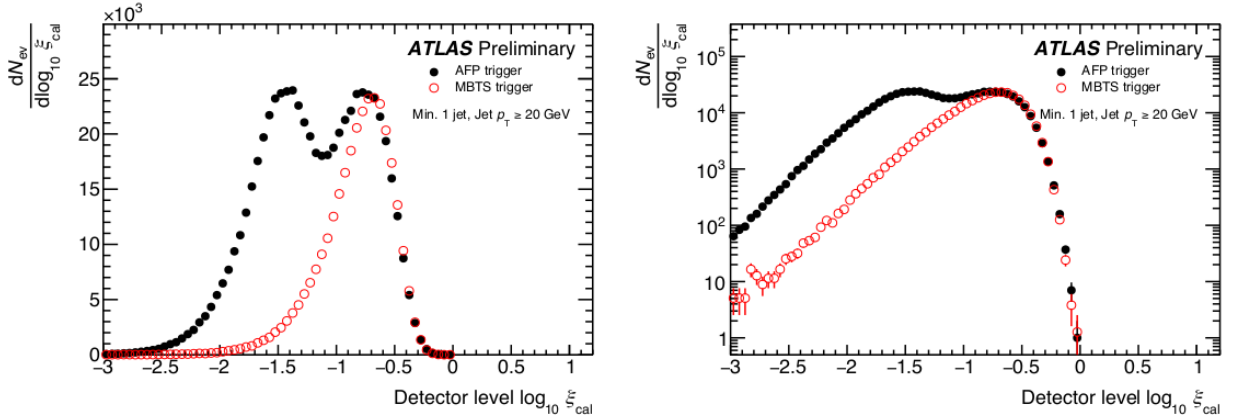


Figure 7.7: The ξ_{cal} distribution in AFP and MBTS data shown on linear (left) and (logarithmic) scale. Events are required to contain at least one jet with $p_T > 20$ GeV and $|\eta| < 3.0$. The MB data sample is normalized to the AFP data in the large ξ_{cal} region. Picture taken from [15].

values which should correspond to the ND contribution. In ideal case two different structures should be possible to identify as in Figure 7.9 where the $x - \xi_{cal}$ correlation can be observed at low ξ_{cal} values. The correlation indicates the presence of diffractive events. Unfortunately we can not observe such a correlation at our results as the consequence of the already discussed large contamination by the non-diffractive background in our selected sample of events. For the means of comparison between Figures 7.8 and 7.9, it is important to note that our distribution is depicted in x -position of the registered tracks and the distribution in Figure 7.9 was obtained from the x -position of the hit pixel [15], our distribution should therefore be mirror turned around the x -axis when compared to the results from [15].

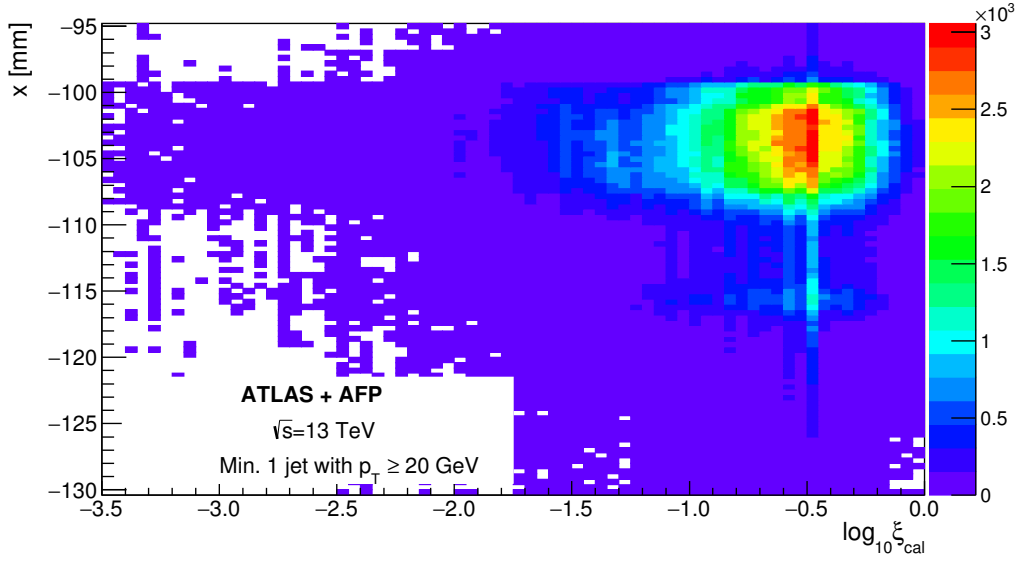


Figure 7.8: A 2D distribution of the x -position of the tracks registered in the AFP Near station ($z = -205$ m) as a function of the ξ_{cal} obtained from the ATLAS calorimeter. Events are required to contain at least one jet with $p_T > 20$ GeV and $|\eta| < 3.0$ and there has to be at least 5 hits in AFP stations in each event.

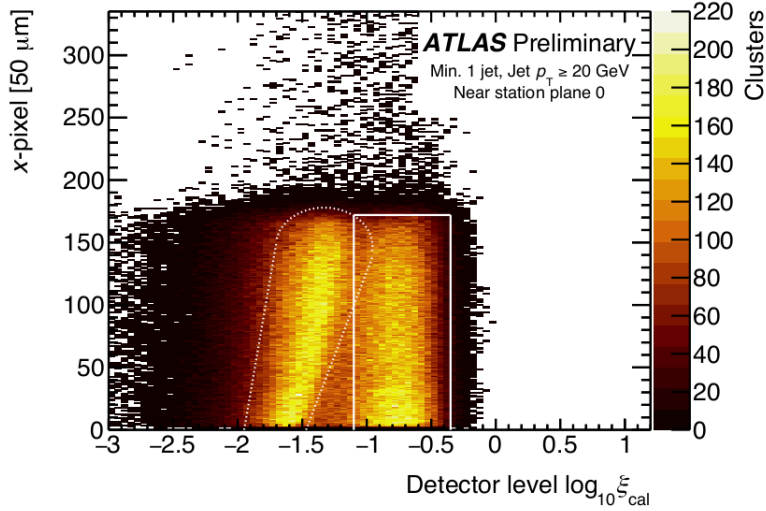


Figure 7.9: A 2D distribution of the x -pixel position in the AFP Near station ($z = -205$ m) as a function of the ξ_{cal} obtained from the ATLAS calorimeter. Events are required to contain at least one jet with $p_T > 20$ GeV and $|\eta| < 3.0$ and there has to be at least 5 hits in AFP stations in each event. Picture was taken from [15].

Finally the distribution of the uncorrected normalized forward rapidity gap size $\Delta\eta_{z<0}^F$ in the AFP-triggered data is depicted in Figure 7.10. Size of the gap is defined as the difference between edge of

the calorimeter acceptance at $\eta = -4.9$ (at the C side in the direction of the AFP detector) and the first occurring particle (most forward calorimeter cluster) with $p_T > 200$ MeV. The distribution shows an exponential tendency due to presence of jets, as has already been observed in the Monte Carlo samples and ATLAS data compared in Chapter 6. The comparison with the $\Delta\eta_{z<0}^F$ distribution from [15] depicted in Figure 7.11 also confirms the previous assumption that our data sample is still highly contaminated with the ND background. There is no tail towards large values of the gap size in Figure 7.10, which would indicate a presence of identified diffractive processes. A visible peak can be observed at $\Delta\eta_{z<0}^F \approx 2$ in Figure 7.10. Although its appearance might suggest the presence of diffractive events in our data sample, we can not confirm such assumption due to high level of the background and pile-up noise which is still present in the selected data.

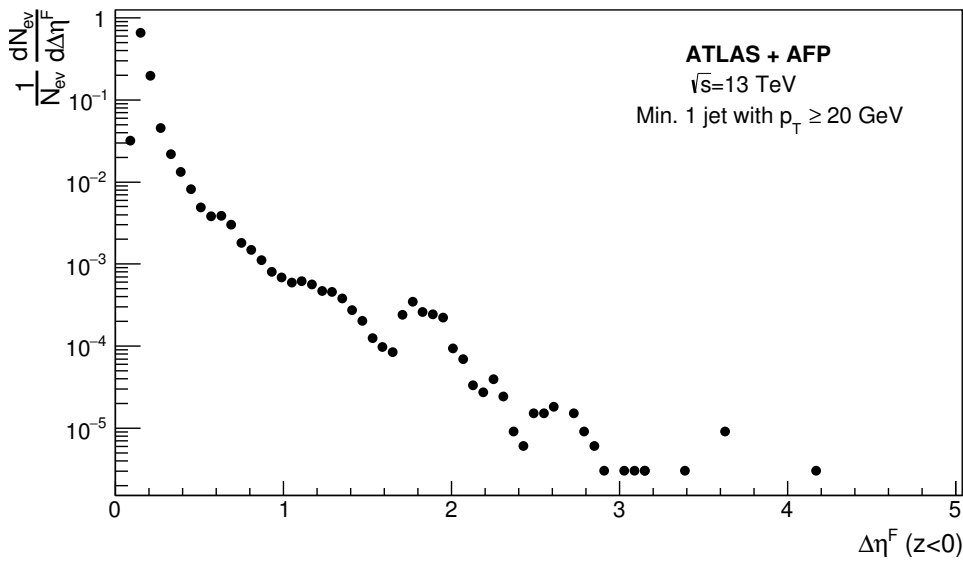


Figure 7.10: Normalized distribution of the detector level $\Delta\eta_{z<0}^F$ in the AFP data samples. Events are required to contain at least one jet with $p_T > 20$ GeV and $|\eta| < 3.0$.

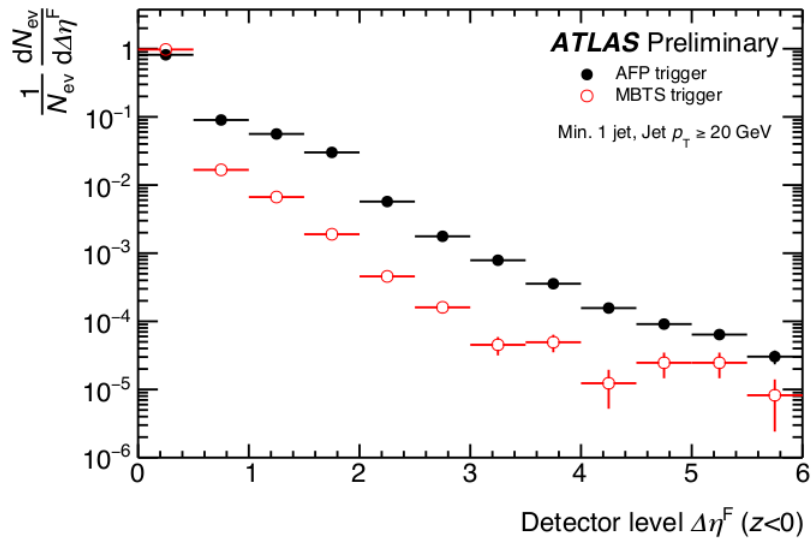


Figure 7.11: Normalized distribution of the detector level $\Delta\eta_{z < 0}^F$ in the AFP and MB data samples. Events are required to contain at least one jet with $p_T > 20$ GeV and $|\eta| < 3.0$. Picture taken from [15].

Conclusion

This project was devoted to the study of diffraction processes. Therefore a summary on the theoretical description of the diffraction was provided. The project was focused on the comparison of the predictions of various version of PYTHIA 8 with the ATLAS data and on the analysis of the ATLAS data triggered using the AFP tracker as a proton tagger. Therefore a short summary on the Monte Carlo generators and PYTHIA was presented. Also the ATLAS and AFP detectors and their main features were described. As we work with the events where the jets are present, a brief description of the jet properties and clustering algorithms was provided.

For the part of the analysis where PYTHIA 8 results are compared, versions 8.1 and 8.2 were used. The main difference of our interest between the two version is that Pythia 8.2 provides a dynamical generation of the gap survival probability factor in hard diffractive events. Events were selected in accordance with the paper [9] using the cut on existence of at least two jets with minimal transverse momentum $p_T > 20$ GeV. The anti- k_t clustering algorithm with the jet radius $R = 0.6$ was used for the jet reconstruction. The Pythia 8.1 predictions and their comparison with the data were studied in detail in the author's bachelor thesis [1], therefore we provide only a brief summary on the topic. We observe an exponential decrease of the total inelastic cross-section with increasing gap size which is governed by the dominant contribution of ND over almost all regions of gap size and no soft survival probability S^2 was needed (i.e. $S^2 = 1.0$) in this particular model. In the next part of the chapter dedicated to PYTHIA 8 predictions, the prediction of Pythia 8.2 performed under the same conditions are presented but we made use of the new option to exclusively generate single diffractive events. Events were generated with the multiparton interactions switched off, the ND contribution has MPI defaultly switched on. Although the ND hard cross-section slightly differs between the two versions of Pythia and therefore different normalization factor had to be used to match the data in the first bin, both versions provide a satisfactory description of the data. This conclusion is confirmed also by the comparison of the ξ distributions. We also examined the effect of the multiparton interactions on the ND component. Switching off the MPI machinery produced ND contribution which did not correspond to the data at all. Therefore we conclude that multiparton interactions are essential for the correct description of the data.

We also presented detector level distributions of the events with jets in the final state. Events were selected using the AFP detector as a proton tagger. Data for this analysis were taken during the dedicated low pile-up run in October 2016. The calorimeter cluster and jet distribution of the p_T showed an expected power-law behavior. Although we could have observed a slight asymmetry in the jet pseudorapidity distribution, the cluster pseudorapidity distribution is symmetric. Therefore we presume that selected events are still contaminated with the background because we expect asymmetric distribution in both calorimeter clusters and jet pseudorapidities with the dominance of positive values of η which correspond to the tagged forward protons in the AFP station at the $z < 0$ side of the ATLAS detector. The fractional momentum loss of the incident proton ξ_{cal} exhibits a clear peak originating from ND contribution.

A small evidence of the second peak originating in single diffractive processes was identified, however the ND background is too significant and therefore SD contribution could not have been confirmed with certainty. The correlation between ξ_{cal} and x -position of the tracks registered in the AFP stations also wasn't confirmed due to the ND background. These assumptions are also confirmed from the detector level forward rapidity gap size $\Delta\eta_{z<0}^F$ which belongs to the rescattered forward proton detected in the AFP at a C side of the ATLAS detector.

Bibliography

- [1] D. Bendova, *Study of diffraction processes at LHC*, Bachelor thesis, 2016.
https://physics.fjfi.cvut.cz/publications/ejcf/BP_Dagmar_Bendova.pdf
- [2] J. Chýla, *Quarks, partons and Quantum Chromodynamics*, University textbook, Prague, 2009.
<http://www-hep2.fzu.cz/Theory/notes/text.pdf>
- [3] P. Růžicka, *Diffraction in the ATLAS Experiment*, Doctoral thesis, 2012.
<http://www-hep2.fzu.cz/~vrba/RuzickaPavel-PhDThesis.pdf>
- [4] S. Donnachie, G. Dosch, P. Landshoff and O. Nachtmann, *Pomeron Physics and QCD*, Cambridge University Press, 2002, ISBN 0-521-78039-X.
- [5] H1 Collaboration (A. Aktas et al.), *Measurement and QCD analysis of the diffractive deep-inelastic scattering cross-section at HERA*, Eur.Phys.J. C48 (2006) 715-748.
- [6] A.D. Martin et al., *Diffractive Physics*, 2012.
arXiv:1206.2124 [hep-ph]
- [7] V.A. Khoze, A.D. Martin, M.G. Ryskin, *Prospects for New Physics observations in diffractive processes at the LHC and Tevatron*, Eur.Phys.J. C23 (2002) 311-327.
- [8] CMS Collaboration, *Observation of a diffractive contribution to dijet production in proton-proton collisions at $\sqrt{s} = 7$ TeV*, Phys. Rev. D 87 (2013) 012006.
- [9] ATLAS Collaboration, *Dijet production in $\sqrt{s} = 7$ TeV pp collisions with large rapidity gaps at the ATLAS experiment*, Phys.Lett. B754 (2016) 214-234.
- [10] V. Kůs, *Study of diffractive processes at the ATLAS Experiment*, Doctoral thesis, 2015.
<http://inspirehep.net/record/1381385/>
- [11] T. Affolder et al. (CDF Collaboration), *Diffractive Dijets with a Leading Antiproton in $\bar{p}p$ Collisions at $\sqrt{s} = 1800$ GeV*, Phys. Rev. Lett. 84 (2000) 5043.
- [12] C. Lefevre, *LHC: The Guide (English version)*, 2009.
<http://cds.cern.ch/record/1165534/files/CERN-Brochure-2009-003-Eng.pdf>
- [13] ATLAS Collaboration, *The ATLAS Experiment at the CERN Large Hadron Collider*, J. Instrum. 3 (2008) S08003.

- [14] ATLAS Collaboration, *Technical Design Report for the ATLAS Forward Proton Detector*, 2015. ATLAS-TDR-024-2015
- [15] ATLAS Collaboration, *Proton tagging with the one arm AFP detector*, 2017. ATL-PHYS-PUB-2017-012
- [16] ATLAS Collaboration, *ATLAS Insertable B-Layer Technical Design Report*, 2010. CERN-LHCC-2010-013
- [17] T. Sjöstrand, S. Mrenna and P. Skands, *A Brief Introduction to PYTHIA 8.1*, JHEP05 (2006) 026, Comput. Phys. Comm. 178 (2008) 852.
- [18] J. Bellm et al., *Herwig 7.0/Herwig++ 3.0 Release Note*, Eur. Phys. J. C (2016) 76: 196.
- [19] M. H. Seymour and M. Marx, *Monte Carlo Event Generators*, Lectures from 69th Scottish Universities Summer School in Physics (SUSSP 69), 2012. arXiv:1304.6677 [hep-ph]
- [20] C. O. Rasmussen, T. Sjöstrand, *Hard Diffraction with Dynamic Gap Survival*, J. High Energ. Phys. (2016) 142.
- [21] B. Isildak, *Measurement of the differential dijet production cross section in proton-proton collisions at $\sqrt{s} = 7$ TeV*, Doctoral thesis, 2012. arXiv:1308.6064 [hep-ex]
- [22] M. Cacciari, G. P. Salam and G. Soyez, *FastJet user manual*, Eur. Phys. J. C72 (2012) 1896.
- [23] M. Cacciari, G. P. Salam and G. Soyez, *The anti- k_t jet clustering algorithm*, JHEP04 (2008) 063.
- [24] T. Sjöstrand et al., *An Introduction to PYTHIA 8.2*, Comput. Phys. Comm. 191 (2015) 159.
- [25] I. Helenius, J. R. Christiansen, C. O. Rasmussen, *Recent PYTHIA 8 developments: Hard diffraction, Colour reconnection and $\gamma\gamma$ collisions*, 2016. arXiv:1604.07996 [hep-ph]
- [26] Pythia 8.1 online manual - Diffraction.
<http://home.thep.lu.se/~torbjorn/pythia81html/Diffraction.html>
- [27] Pythia 8.2 online manual - Diffraction.
<http://home.thep.lu.se/~torbjorn/pythia82html/Diffraction.html>
- [28] Documentation of the ROOT data analysis framework.
<https://root.cern.ch/documentation>
- [29] Internal Twiki page of the AFP project in the ATLAS experiment. <https://twiki.cern.ch/twiki/bin/view/Atlas/AFP>